Equilibrium Structure and Dynamics of the California Current System

PATRICK MARCHESIELLO, JAMES C. MCWILLIAMS, AND ALEXANDER SHCHEPETKIN

Institute of Geophysics and Planetary Physics, University of California, Los Angeles, Los Angeles, California

(Manuscript received 13 November 2001, in final form 2 October 2002)

ABSTRACT

This paper addresses the structure and dynamical mechanisms of regional and mesoscale physical variability in the subtropical northeast Pacific Ocean using the Regional Oceanic Modeling System (ROMS). The model is configured with a U.S. West Coast domain that spans the California Current System (CCS) with a mesoscale horizontal resolution up to as fine as 3.5 km. Its mean-seasonal forcing is by momentum, heat, and water fluxes at the surface and adaptive nudging to gyre-scale fields at the open water boundaries. Its equilibrium solutions show realistic mean and seasonal states and vigorous mesoscale eddies, fronts, and filaments. The level of eddy kinetic energy (EKE) in the model is comparable to drifter and altimeter estimates in the solutions with sufficiently fine resolution. Because the model lacks nonseasonal transient forcing, the authors conclude that the dominant mesoscale variability in the CCS is intrinsic rather than transiently forced. The primary eddy generation mechanism is the baroclinic instability of upwelling, alongshore currents. There is progressive movement of mean-seasonal currents and eddy energy offshore and downward into the oceanic interior in an annually recurrent cycle. The associated offshore eddy heat fluxes provide the principal balance against nearshore cooling by mean Ekman transport and upwelling. The currents are highly nonuniform along the coast, with important influences by capes and ridges in both maintaining mean standing eddies and launching transient filaments and fronts.

1. Introduction

The continental U.S. West Coast (USWC) abuts a collection of eastern boundary currents called the California Current System (CCS). Theoretical and modeling studies of the CCS have traditionally focused on the coastal upwelling and downwelling processes in response to the strong alongshore winds over the narrow continental shelf. More recently, a focus has also been made on the broad equatorward flow in the offshore region, motivated by satellite and drifters observations of shelf water streaming offshore at many locations along the coast. These observations indicate that intrinsic variability of the persistent currents plays an important role in cross-shore transport of material properties that have human importance for fisheries, water quality, shoreline control, and shipping operations.

The Regional Oceanic Modeling System (ROMS; Shchepetkin and McWilliams 2003, hereinafter SMA; A. Shchepetkin and J. C. McWilliams 2003, unpublished manuscript, hereinafter SMB) was developed to simulate such phenomena. Its computational methods, parallel architecture, and robust open-boundary conditions (Marchesiello et al. 2001) allow for realistic, long-term integrations in a fine-mesh regional domain. Few other realistic regional simulations have been made for the USWC, and the modeling studies mostly have used simplified dynamics, domains, and forcing, with coarser spatial resolution or/and shorter integration times. In this paper we report on ROMS simulations of the equilibrium, seasonal-cycle, USWC circulation that are of interest both for the mean-seasonal circulation itself and as a clean demonstration of intrinsic circulation variability that arises from instabilities of the persistent currents in the absence of added forced variability by synoptic and interannual atmospheric fluctuations.

2. Oceanographic conditions and dynamics

Many field observations have been made along the USWC. Since 1950 the California Cooperative Ocean Fisheries Investigation (CalCOFI) has provided a large-scale time series of hydrographic measurements off central and southern California. In the northern part of the USWC, a series of process experiments [Coastal Upwelling Experiment (CUE), Coastal Transition Zone (CTZ), Eastern Boundary Current (EBC), Coastal Ocean Dynamics Experiment (CODE), Coastal Ocean Processes (CoOP), Global Ocean Ecosystem Dynamics (GLOBEC)] have been made with shipboard hydrographic and Doppler current surveys, plus moored arrays and Lagrangian drifter arrays to sample both large-scale and mesoscale currents. Satellite measurements of sea surface temperature (SST) [Advanced Very High

Corresponding author address: Dr. Patrick Marchesiello, IGPP, University of California, Los Angeles, 405 Hilgard Avenue, Los Angeles, CA 90095-1567.
E-mail: patrickm@atmos.ucla.edu

Resolution Radiometer (AVHRR)], sea surface height η (altimetry), and color (SeaWIFS) give more extensive coverage but are limited to only the surface. Theoretical and computational models have provided useful paradigms for the dynamics of the CCS. A recent review of observations, laboratory experiments, and model results on the CCS can be found in Hickey (1998), and a collection of the most recent CCS observations is in special issues of *Deep-Sea Research* (2000, vol. 47B, 761–1176) and *Progress in Oceanography* (2002, vol. 53, nos. 2–4).

In the northeast Pacific Ocean the west-wind drift meets the coast at around latitude 45°N and separates into two eastern-boundary current systems: the Alaska Current System and the CCS. In the traditional view the CCS consists of several large-scale currents. The broad, slow, equatorward California Current (CC) overlies the poleward California Undercurrent (CUC). There is also a spring/summer equatorward coastal current and a wintertime poleward coastal current, known as the Davidson Current (DC). The CCS contains three characteristic water masses: Pacific Subarctic Water (low salinity *S* and temperature *T*, high oxygen and nutrients) is advected equatorward with the coastal current; North Pacific Central Water (high *S*, *T*, and nutrients; low oxygen) enters from the west with the west-wind drift; and southern water (high *S* and *T*, low oxygen and nutrients) comes from the south with the CUC. In general, *S* and *T* increase equatorward in the CCS. Salinity also increases with depth in the CCS, thereby enhancing the baroclinicity (i.e., as opposed to the Benguela Current system, another subtropical, eastern-boundary upwelling regime). In addition, a surface, low-*S* tongue of equatorward flowing water, composed of Pacific Subarctic Water and inflows from the Columbia and other rivers, forms off the USWC between upwelled southern water at the coast and North Pacific Central Water.

The CC is generally defined as an equatorward surface current about 1000 km wide and 500 m deep, with a peak speed of 10 cm s^{-1}. This appears consistent with the Sverdrup transport mechanism (Sverdrup 1947) relating negative wind curl and equatorward oceanic currents. By the same mechanism, we expect a nearshore poleward current since the wind field off California has a positive wind curl within 200 km of the coast (Bakun and Nelson 1991), which may partly explain the presence of the DC in the winter (Munk 1950). In the spring strong, equatorward, alongshore winds are favorable for coastal upwelling and overwhelm the effect of the wind curl (McCreary et al. 1987), creating a strong equatorward coastal jet and associated poleward CUC. Although alongshore, coastal winds are the dominant forcing from the northern tip of Washington (48°N) south to Point Conception (35°N) in southern California, there is a significant difference north and south of 40°N. During summer the alongshore winds are favorable for coastal upwelling but are more variable north of 40°N. During winter low pressure systems from the Gulf of Alaska cause a strong northward component in the coastal winds and downwelling along the coast of Oregon and Washington, while upwelling generally continues intermittently south of San Francisco (37°N), interrupted by occasional winter storms. Relaxation of the local equatorward winds results in a pressure gradient force that can drive a transient, poleward current, which is another proposed mechanism for the DC (McCreary et al. 1987). In the Southern California Bight (SCB), between Point Conception and the U.S.–Mexico border, interactions between remotely forced currents and topography are dominant, and weak local winds are often only a secondary forcing (Hickey 1992). The CUC can be interpreted as a companion to the surface, equatorward, coastal jet, both of which are associated with the formation of coastal upwelling fronts. The CUC is relatively narrow (10–40 km) and flows poleward over the continental slope all along the USWC, transporting warm, salty southern water (Hickey 1998). It is strongest at depth 100–300 m. As for the surface jet, the CUC can be continuous over long distances (Pierce et al. 2000) or break into separating, mesoscale jets with peak speeds of 30–50 cm s^{-1} (Cornuelle et al. 2000; Barth et al. 2000). CalCOFI hydrography (Lynn and Simpson 1987) and satellite altimetry (Kelly et al. 1998; Strub and James 2000) show that the CCS has high seasonal variability, both in response to seasonal wind forcing and as Rossby wave propagation. The seasonal pattern is generally described as the evolution of a coastal jet that forms during upwelling favorable springtime and then moves off the shelf to become a deep-ocean CC flow out to approximately 130°W, where its surface energy abates between fall and spring.

Recent observations show that both offshore and nearshore currents are quite energetic in the CCS. Nearshore currents are responsive to local wind forcing and remote influences transmitted along the coastal waveguide. They develop into strong southward jets during upwelling season, with significant topographically modulated variability (Song et al. 2002, manuscript submitted to *J. Phys. Oceanogr.*, hereinafter SON; Barth et al. 2000). Offshore currents have intrinsic mesoscale variability from instabilities of the persistent alongshore currents, some of which emerge from the nearshore region and are weakly related to local fluctuations of the wind stress (Kelly et al. 1998). Satellite images often show sharp cross-shore gradients in SST and color, indicating a barrier to material exchanges, but they also show episodic filamentary intrusions across the barrier from both sides. This pseudo barrier has therefore been identified as the coastal transition zone, about 300 km wide. The existence of a coastal transition zone in the CCS is associated with a short shelf-flushing time by cross-shelf transport of only a few days. In contrast, off the North American east coast, flushing times are much longer, up to years (Brink 1998) because the shelves are relatively broad and the transport mechanisms are essentially related to cross-isobath penetration events by

strong western boundary currents. This penetration seldom reaches the shelf areas, and shelfbreak fronts separating nearshore and offshore waters are commonly observed. Off the USWC the important cross-shelf transport mechanisms are the Ekman transport and the effects of topography and instabilities on the alongshore coastal jets. The ageostrophic, offshore Ekman transport is perpendicular to the coast during the summertime upwelling regime. The topographic effect on the wind-driven coastal circulation is shown by Narimousa and Maxworthy (1989) to form local upwelling centers and standing waves with cross-shore transports. Instability of the coastal jets does not require topographic effects (McCreary et al. 1991), but capes (Batteen 1997) and ridges (SON) may promote locally enhanced cross-shore transport. An important aspect of eastern-boundary current systems is also related to Rossby wave dynamics, which transport energy westward to the open ocean (McCreary and Kundu 1985). The offshore progression of Rossby waves also affects the vertical structure of coastal currents, hence their instability characteristics and their separation from the coast as filaments, especially around capes and ridges.

Because nearshore and offshore currents have distinctive spatial scales, O(1–10) km nearshore and O(100–1000) km offshore, they are usually both measured and modeled with separate methods, with an implicit assumption that their interactions are weak. Few realistic regional simulations have been made for the USWC, and the modeling studies mostly have used simplified dynamics, domains, and forcing, with coarse spatial resolution or/and short integration times. These studies nonetheless have implicated the primary mechanisms for seasonal, mesoscale, and submesoscale variability of the CCS (i.e., wind forcing, Kelvin waves and Rossby wave propagation, and a large range of instability processes). The model results of Batteen (1997) indicate, consistent with observations, that much of the seasonal cycle in the CCS is a deterministic response to the forcing, with phase and amplitude shifts due to Rossby waves. Strong intrinsic variability has been seen in many numerical solutions (Ikeda et al. 1984; Auad et al. 1991; McCreary et al. 1991; Haidvogel et al. 1991; Pares-Sierra et al. 1993; Batteen 1997). Quasigeostrophic models implicate baroclinic instability as the cause of variability of offshore currents; however, they lack the ability to produce sharp fronts and their associated instabilities. In this context, our goal is to simulate the mean-seasonal equilibrium CCS with realistic dynamics, forcing, and domain configuration and with sufficient spatial resolution to include intrinsic mesoscale variability and some aspects of shelf–offshore interaction.

3. The model

a. Background

Coastal oceanic models achieved robustness and reliability in the late 1980s with some essential features incorporated in the Princeton Ocean Model (POM; Blumberg and Mellor 1987): incompressible, hydrostatic primitive equations; free surface with time splitting for barotropic and baroclinic modes; terrain-following vertical coordinate (σ); and boundary layer parameterization. In particular, the σ coordinate is thought to better capture the important interactions between bottom topography and ocean dynamics in coastal regions than the traditional height coordinate (Lott et al. 1990; Marchesiello et al. 1998). However in the 1990s, when trying to extend this class of models over the continental slope to the open ocean, a new set of problems appeared (Barnier et al. 1998). The greatest model errors are essentially related to the σ coordinate: truncation errors from the horizontal pressure gradient operator and substantial diapycnal mixing from improper formulation of the mixing tensor and advection. New algorithms for coordinate transformation were devised and some limits of validity were estimated and used to smooth the topography. These developments were incorporated in later versions of the S-Coordinate Primitive Equation Model (SPEM: Haidvogel et al. 1991) and the S-Coordinate Rutgers University Model (SCRUM: Song and Haidvogel 1994).

At present some of the greatest limitations in regional modeling are related to spatial extent and resolution, since the purpose is to model both coastal and oceanic regions and their interactions. An element of the latter is open-boundary conditions that permit stable, long-term integration of a regional model to study its equilibrium behavior in a sufficiently small domain so that computational resources are used to increase the model's spatial resolution rather than extend the domain.

b. Equations and discretizations

ROMS is an evolutionary descendent from SCRUM. It solves the incompressible, hydrostatic, primitive-equation model with a free sea surface, horizontal curvilinear coordinates, and a generalized terrain-following vertical coordinate that can be configured to enhance resolution at the sea surface or seafloor. The prognostic variables are surface elevation η, barotropic horizontal velocity components ($\overline{u}$, $\overline{v}$), baroclinic horizontal velocity components (u, v), and material properties such as T and S. The *UNESCO Equation of State* is implemented using potential rather than in situ T. The open-boundary conditions are a combination of outward radiation and flow-adaptive nudging toward prescribed external conditions (Marchesiello et al. 2001, further described below).

The model has been designed to use parallel computer architectures, allowing us to solve much larger problems than with the serial code. ROMS has been designed for shared-memory computer architectures such as the SGI/Cray Origin 2000. Parallelization and optimal use of processors caches (local fast memory) are done simultaneously by an explicit two-dimensional partitioning

into subdomains. Multiple subdomains are assigned to each processor so the data blocks fit into the processor cache. Sixty-four processors were used for the USWC calculation at 5-km resolution ($256 \times 512 \times 20$ grid points), requiring about 30 wall-clock hours to complete a year's simulation.

The finite-difference discretization algorithms are oriented toward nonoscillatory, high-order schemes, thus improving the effective resolution of the model (weighing accuracy against computational cost; see, e.g., Sanderson 1998). Once a grid resolution passes a certain threshold with viscosity decreased accordingly, the simulated flow becomes turbulent. Experience in computational fluid dynamics for turbulent flows has shown that conventional, second-order, discretized advection schemes are not satisfactory in comparison with higher-order schemes. In ROMS the advection operator is third order and upstream biased, designed to reduce dispersive errors and the excessive dissipation rates needed to maintain smoothness, thereby effectively enhancing the resolution on a given grid (Shchepetkin and McWilliams 1998). The pressure gradient formulation used in the simulations reported here is a variation of the density Jacobian formulation of Song (1998), with an optimized correction for vertical grid stretching. The vertical mixing in the interior and planetary boundary layers is calculated with the nonlocal, K-Profile Parameterization scheme (KPP: Large et al. 1994) that performs well in both measurement comparisons and large-domain model solutions (Large and Gent 1999; Li et al. 2001), and was adapted to the C-grid structure of ROMS.

A mode-splitting technique allows the separation of the barotropic and baroclinic components in the model with internal and external time steps. The mode splitting is done using a time filter, which ensures that the continuity equation is satisfied on the discrete level, thus removing previous restrictions of small free-surface changes. The time stepping is a leapfrog/Adams–Moulton, predictor–corrector scheme, which is third-order accurate in time and has good dispersive properties for the advection equation. An expanded regime of stability allows larger time steps. The vertical diffusion terms are treated with an semi-implicit, Crank–Nicholson scheme to avoid time step restrictions due to large vertical mixing rates in the boundary layers and in the interior when static stability needs to be restored. The reader is referred to SMA and SMB for a more complete report.

c. Configuration and forcing

In the USWC configuration the domain extends in latitude from the middle of Baja California (~28°N) to the Canadian border (~48°N, approximately coincident with the subtropical/subpolar gyre boundary). This is about 2000 km alongshore and 1000 km offshore, and it encompasses the CCS and its most energetic eddy regions. The model time step is 15 min; the horizontal grid spacing varies among cases from 3.5 to 20 km (note that at 5-km resolution there are 256×512 grid points); and the vertical grid has 20 levels with surface refinement. The stretching parameters for the vertical grid (Song and Haidvogel 1994) are $\theta_S = 7$ and $\theta_B = 0$ to allow for a reasonable representation of the surface boundary layer everywhere in the domain. The topography of the model is obtained by bilinear interpolation of the ETOPO5 analysis (NGDC 1988). Depths shallower than 50 m are reset to 50 m. After interpolation and truncation, the topography is smoothed using a selective Shapiro filter for excessive topographic parameter values (Beckmann and Haidvogel 1993) to avoid large pressure gradient errors. The required degree of smoothing is estimated by integrating the model without forcing and with closed-boundary conditions (Barnier et al. 1998): where erroneous currents are generated over steep slopes, the topography is selectively smoothed until those errors become much smaller than the actual currents to be simulated. Note that limited model resolution and associated smoothing requirements may affect our representation of the USWC narrow continental shelf, although resolutions of 3.5 and 5 km allow, respectively, for nine and six computational points in the shelf zone.

Model initialization is with Levitus et al. (1994) and Levitus and Boyer (1994) T and S for the month of January and no flow. Winter is a period of minimum wind forcing and current energy in a monthly mean sense, which reduces initial spinup problems. The surface forcing is by mean-seasonal wind stress, heat, and freshwater flux derived from the Comprehensive Ocean–Atmosphere Data Set (COADS) (da Silva et al. 1994). This mean-seasonal forcing formulation is better suited to a fundamental investigation of the eastern-boundary system as a whole than to particular nearshore sites dominated by synoptic forcing. Except for solar radiation, the total heat flux Q is applied to the surface grid level and formulated as in Barnier et al. (1995). A correction with respect to surface T, dQ/dT derived from bulk formulas, is used to introduce thermal feedback:

$$Q = Q_{\text{obs}} + \frac{\delta Q}{\delta T}(T_{\text{model}} - T_{\text{obs}}). \tag{1}$$

The heat flux sign convention is positive downward. The correction is a simple representation (using a truncated Taylor series about the surface T) of the thermal feedback of the ocean surface temperature to the flux at the air–sea interface. The same correction is used for surface (virtual) S flux since direct measurements of evaporation and precipitation are sparse. The S flux correction also provides a parameterization of the important Colombia River runoff along the Washington coast, which produces surface S minima a few hundred kilometers down the coast. The solar radiation flux is treated separately because its vertical variations influence sig-

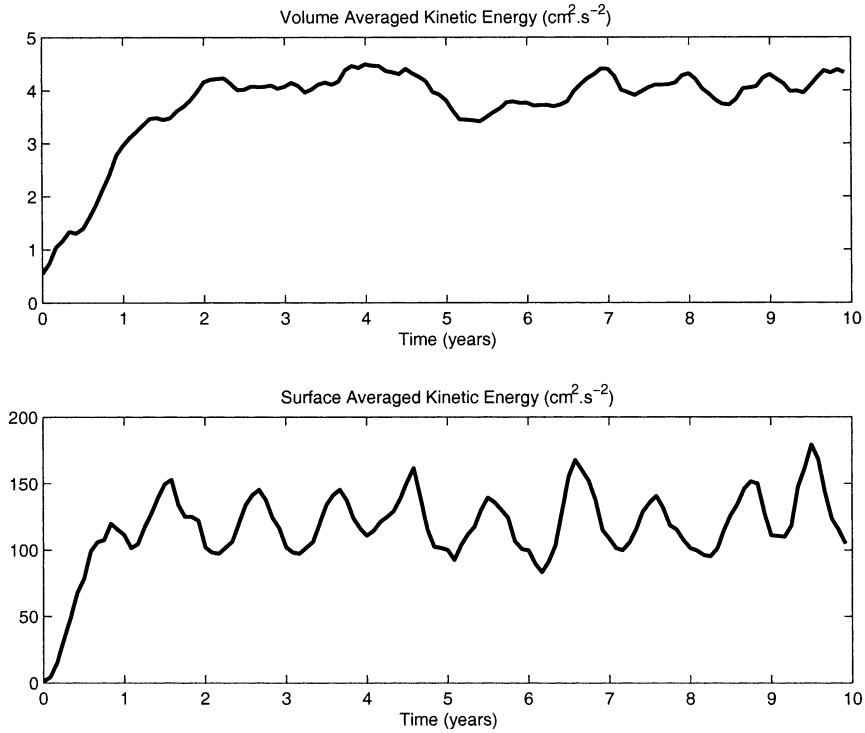

FIG. 1. Time evolution of the (top) volume-averaged KE ($cm^2\ s^{-2}$) and (bottom) surface KE from the model with 5-km resolution.

nificantly the mixed layer dynamics (Large et al. 1994).[1] The insolation Q_S is used as a forcing function for both the T equation and for the surface layer submodel. It is a penetrative flux fractionally partitioned into two frequency bands with absorption coefficients corresponding to the first Jerlov water type (Paulson and Simpson 1977):

$$Q_S(z) = 0.57e^{z/0.35\ \mathrm{m}} + 0.43e^{z/23\ \mathrm{m}}. \quad (2)$$

The first (high frequency) band is quickly absorbed at the surface, while the second band of visible light (photosynthetically available radiation) can penetrate the surface layer.

There are open boundaries at the western, northern, and southern borders. Often the flow and dominant waves are in opposite directions. Rossby waves transport eddy kinetic energy (EKE) to the west against the west-wind drift, low-frequency coastally trapped waves propagate northward against the CC and with the CUC, and gravity waves are omnidirectional. Therefore, the open-boundary conditions are rather delicate in this region. Levitus et al. (1994) mean-monthly T and S and COADS winds were used to estimate climatological values for the geostrophic and Ekman baroclinic velocity components; a level of no motion at depth 500-m was assumed to determine the total velocity. This climatology is used at open boundaries for all prognostic variables following the method described in Marchesiello et al. (2001). An oblique radiation condition is used to estimate the direction of information flux at the open boundaries; if the direction is inward, a nudging term quickly restores the climatological values (timescale $\tau_{\mathrm{in}} = 1$ day), otherwise the radiation condition is used to extrapolate interior values at boundary points in addition to a weak nudging ($\tau_{\mathrm{out}} = 1$ yr). To enforce volume conservation and avoid accumulative dynamical errors, a constraint to the barotropic mode is added. The model also uses sponge layers and weak nudging layers (τ_{out} maximum). The values of the sponge and nudging parameters vary as the half cosine function from a maximum at the boundary to zero at the inner edge of the layer; the layer width is set to 150 km (i.e., on the order of mesoscale structures); the maximum viscosity (diffusivity) values for the sponge layers are 100 (50) $m^2\ s^{-1}$.

4. Equilibrium solutions

The model is integrated for 10 years except at the highest resolution of 3.5 km. After a spinup period of about 2 years, the surface kinetic energy (KE; Fig. 1) oscillates quasiperiodically around an equilibrium value. The volume-integrated KE does not show a clear

[1] The mixing layer dynamics are also sensitive to diurnal variations of solar radiation and more importantly to synoptic winds according to some of our experiments (not presented here). The synoptic winds effect is to deepen the mixing layer depth, particularly offshore and north of 37°N in winter (storm period). However, we found this not to affect significantly our present results on the dynamics of the CCS.

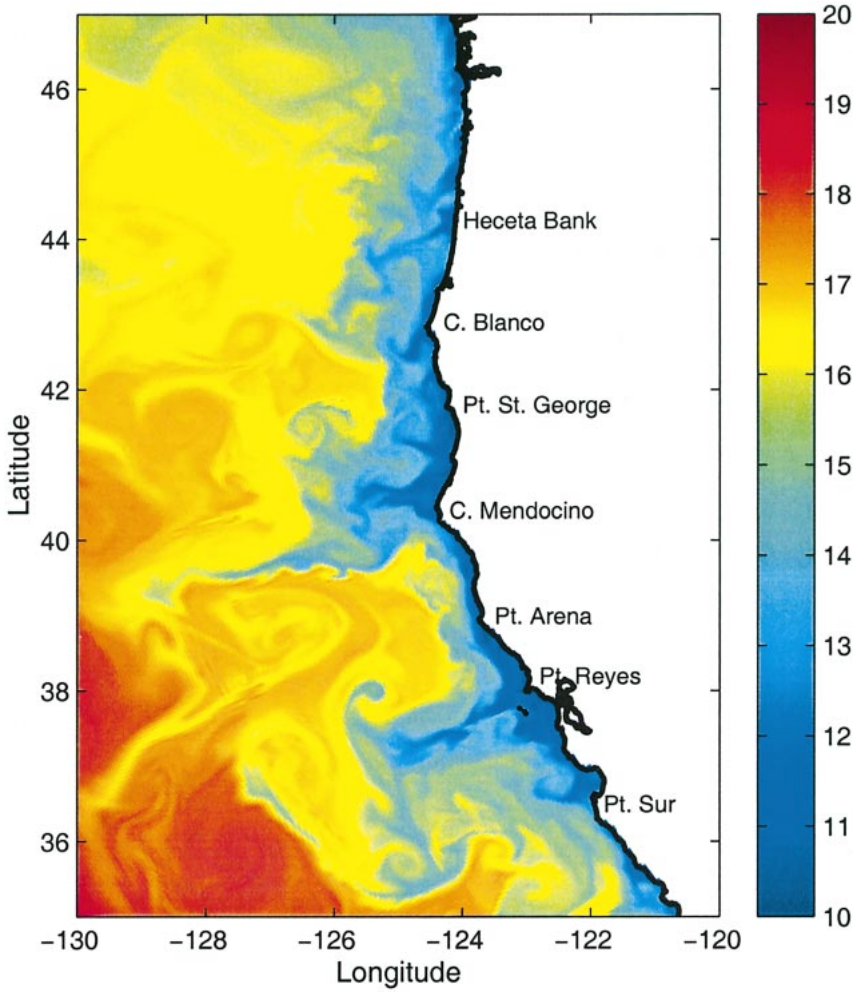

FIG. 2. Upwelling filaments in SST (°C) in late summer off the central USWC from the model with 3.5-km resolution.

seasonal cycle, although it does exhibit interannual variability as an indication of intrinsic variability. The difference between these KE measures is an indication that the offshore energy decay occurs as much by burial as by dissipation. We analyze the period from year 3 to year 10 over which all annual-mean and seasonal-mean fields are examined. Our main focus is on the principal upwelling region, which we define as extending from Point Conception to Cape Blanco.

a. General description

We first give a phenomenological description of the solution behavior, as a prelude to a statistical analysis of the equilibrium state. For this purpose, we also include a solution of the model at a high resolution of 3.5 km, integrated nearly to equilibrium (3 years) but not sufficiently long for statistical analysis. The 3.5- and 5-km simulations exhibit very similar patterns although they differ in the greater amount of small-scale eddies (~20 km) seen in the higher-resolution case. We attribute these eddies to a short-wavelength, ageostrophic frontal instability, only marginally resolved even at our finest resolution [section 4e(2)].

The simulations have mesoscale variability patterns in SST, especially the highly visible cold filaments (Fig. 2), that resemble satellite images (Strub et al. 1991). Near-surface mesoscale variability is spatially and temporally organized by the seasonal wind. In spring frontal instabilities appear along the newly formed coastal current and roll up into cyclonic vortices. Most filaments occur in summer, associated with strong squirts (~1 m s^{-1}) forming both cold and warm, mushroom-shaped patterns at multiple scales (Figs. 2 and 3), especially south of Cape Blanco. In autumn, meanders and eddies are the dominant patterns, both inshore and offshore of the CC. In winter, the offshore eddy field is strongest. There is significant vertical motion within the cold filament that impacts the PBL with evident patchiness in its depth (Fig. 3b) and the associated vertical mixing intensity.

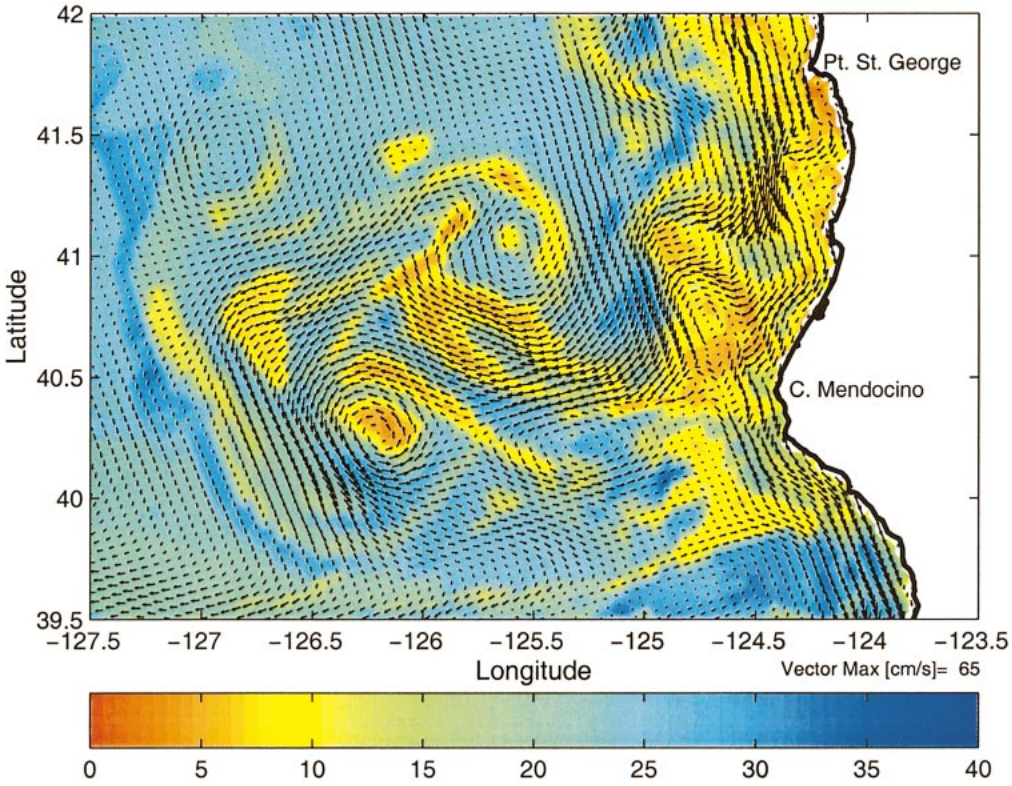

FIG. 3. Upwelling filament in surface boundary layer depth (m) and currents off Cape Mendocino in late summer from the model with 3.5-km resolution.

Hammerheads or mushroom-shaped SST patterns are caused by counterrotating dipole eddies (Mied et al. 1991). In the CCS the surface expression of the largest dipoles (~200 km) consists of strong, low pressure, cyclonic and weak, high pressure, anticyclonic vortices; peak velocities are about 1 m s^{-1} (Fig. 4; note the deeper lows in cyclones, with sea surface height anomalies below −16 cm, in comparison with the weaker highs in the anticyclonic eddies, between 4 and 8 cm). At depths representative of the CUC (typically near $\sigma_t = 26.6$ kg m^{-3}, at about 250-m depth offshore), the situation is reversed with strong, anticyclonic and weak, cyclonic vortices and peak velocities of 0.25 m s^{-1} (Fig. 4). The flow structures systematically propagate westward allowing offshore transport and mixing of their respective material properties (Chereskin et al. 2000). Although observations of dipole eddy pairs are difficult because the surface signal of anticyclones is weak, their presence has been reported along the northern part of the USWC (Ikeda et al. 1984; Thompson and Papadakis 1987) and off southern California (Simpson and Lynn 1990), where the subsurface *S* signal is particularly strong. Cornuelle et al. (2000) traced a deep, offshore, anticyclonic eddy carrying southern water from the coastal regions of northern California. The dipoles result from instability of coastal surface and subsurface currents that, respectively, form the cyclonic and anticyclonic eddies. Note that while surface currents and undercurrents have opposite directions along the coast, they seem to merge in the separation process into single squirts. As a result, the cross-shore currents associated with the filaments have a deeper structure than the nearshore currents. On the shelf, the variability is on a smaller scale and often appears as small cyclonic eddies with connections to the larger offshore mesoscale vortices, particularly during the upwelling season. We already mentioned the presence of small eddies (~20 km) that emerge in the 3.5-km simulation (cf. Figs. 2 and 5). These submesoscale patterns are fast growing and concentrated in the upper water column (<50 m), as opposed to the deeper mesoscale eddies.

Figure 5 presents a snapshot of SST at the end of summer for four consecutive years. There is considerable interannual variability in the production of the filaments, but we also note consistencies as part of the annual cycle. SON analyze the present model solution in a process study of cross-shore transport and show that filaments occur preferentially at locations corresponding to topographic features. Most are found south of Cape Blanco, Point St. George, Cape Mendocino, Point Arena, and Point Reyes. There is also a meander formed north of Cape Blanco at Heceta Bank where separating coastal jets are commonly observed (Oke et

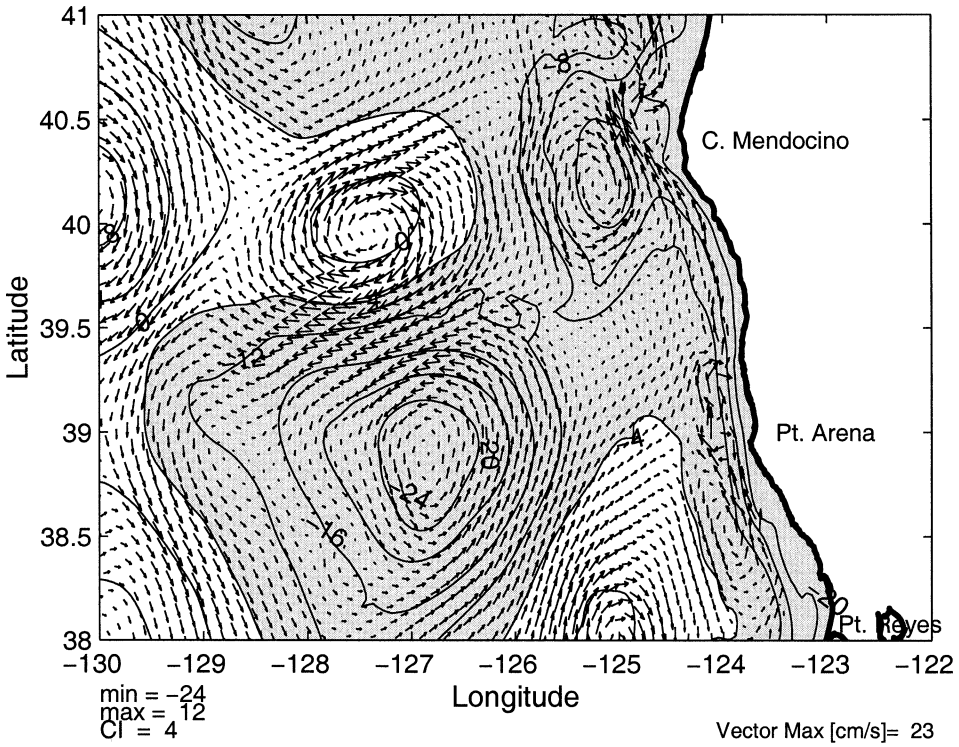

FIG. 4. SSH (cm) and currents at depth 250 m off Cape Mendocino in late summer from the model with 3.5-km resolution. Note in particular the antisymmetry of flow speed in surface and subsurface layers of cyclonic and anticyclonic circulations. Negative values for the sea level are shaded.

al. 2002). The filaments develop through instability of the seasonally wind-driven coastal currents and therefore may be partially predictable.

b. Persistent currents

1) STANDING EDDIES

The simulated, annual-mean sea surface height (SSH) is shown in Fig. 6a along with the surface dynamic height relative to 500 dbar from the Levitus et al. (1994) climatological analysis (Fig. 6d). At the largest scales the two fields are quite similar, in part because the latter is used in the model's boundary conditions. The westwind drift flows from the west toward the coast and turns south as the broad CC. In the Levitus analysis the CC is somewhat closer inshore and extends farther north than in the model. At smaller scales there are obvious differences particularly in the coastal transition zone. The model produces a coastal current with large steady meanders (i.e., standing eddies), that extend offshore from some of the major ridges, such as Cape Mendocino, Point Reyes, and Point Conception (cf. Narimousa and Maxworthy 1989; SON). Observations confirm the presence of quasi-permanent standing eddies; for example, Lagerloef (1992) identifies a recurrent, summer, anticyclonic Point Arena eddy between two cyclonic meanders at Cape Mendocino and Point Reyes; in long-term mean CalCOFI data, Wyllie (1966) and Hickey (1979) also identify semipermanent eddies respectively off Point Conception and Monterey.

The Levitus analysis is spatially quite smooth, with a decorrelation scale on the order of 1000 km, and its surface height estimate is not an absolute one, lacking a reference-level field. To partly bridge these differences, the simulated dynamic height relative to 500 m is shown in Fig. 6c. In comparison with the SSH, the alongshore variability in the dynamic height is much smaller and the CC is closer to the coast, both of which make it more like the Levitus analysis. This indicates that the cross-shore currents are relatively deep and alongshore currents are shallow relative to 500 m. Furthermore, the majority of the hydrographic measurements in the CCS are made during the upwelling season, thereby biasing the annual-mean estimation. For this comparison we show the simulated, summer-mean SSH (Fig. 6b), which shows the CC as a stronger, nearer-shore circulation along the whole USWC, especially in the north. Thus, there is general consistency between the simulated and measured mean CCS.

2) CROSS-SHORE STRUCTURE

To examine the subsurface circulation we focus on a central upwelling region with quasi-homogeneous alongshore conditions, from Point Conception north to Cape Blanco. The excluded northern part is subject to

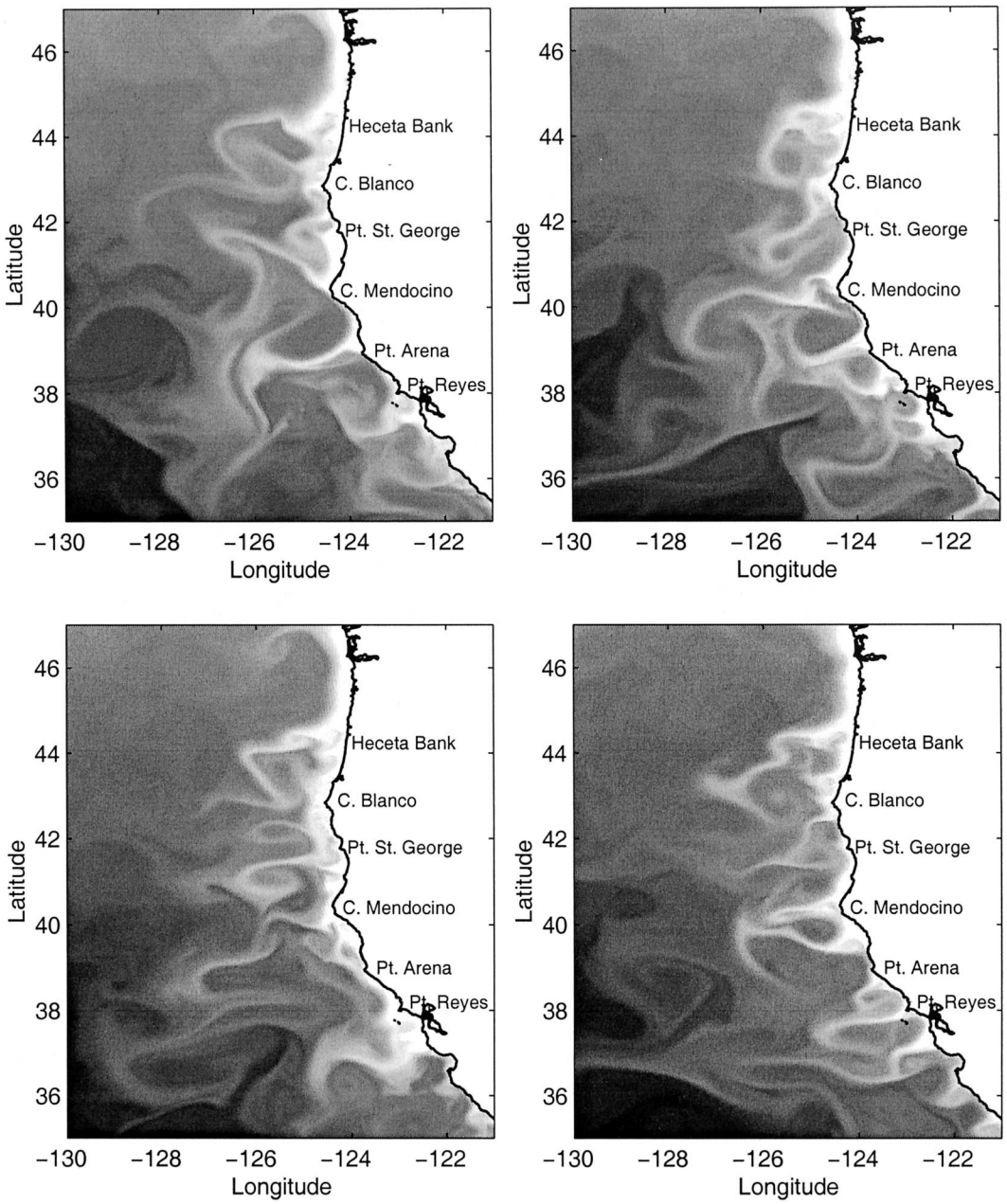

FIG. 5. Upwelling filaments in SST off the central USWC in late summer (30 Sep) for four consecutive years (years 7–10) from the model with 5-km resolution.

strong seasonal downwelling as the subpolar gyre shifts southward in wintertime, and the SCB has a peculiar local circulation strongly influenced by its complex island and basin topography and influential remote forcings. Within the upwelling region we make an alongshore average along all horizontal lines equidistant to the shoreline.

Figure 7 shows the mean cross-shore structure of the CCS in the upwelling region. The nearshore, equatorward jet has a maximum speed of 18 cm s^{-1} and is about 100 m deep; the CUC occurs between about 50 and 1000 m, with a peak speed of 5 cm s^{-1} around 150–250 m. These values are in good agreement with estimates from the Calcofi climatology of the alongshore, geostrophic currents off central California (Chelton 1984). The coastal upwelling front in T and S rises to the surface between these currents (Figs. 7b,c). The offshore system can be recognized as the traditional CC—that is, a broad, weak, equatorward drift in the upper few hundred meters, which imprints two surface salinity minima around 100 and 300 km offshore. Also seen is a deep, broad, weak, poleward subsurface current be-

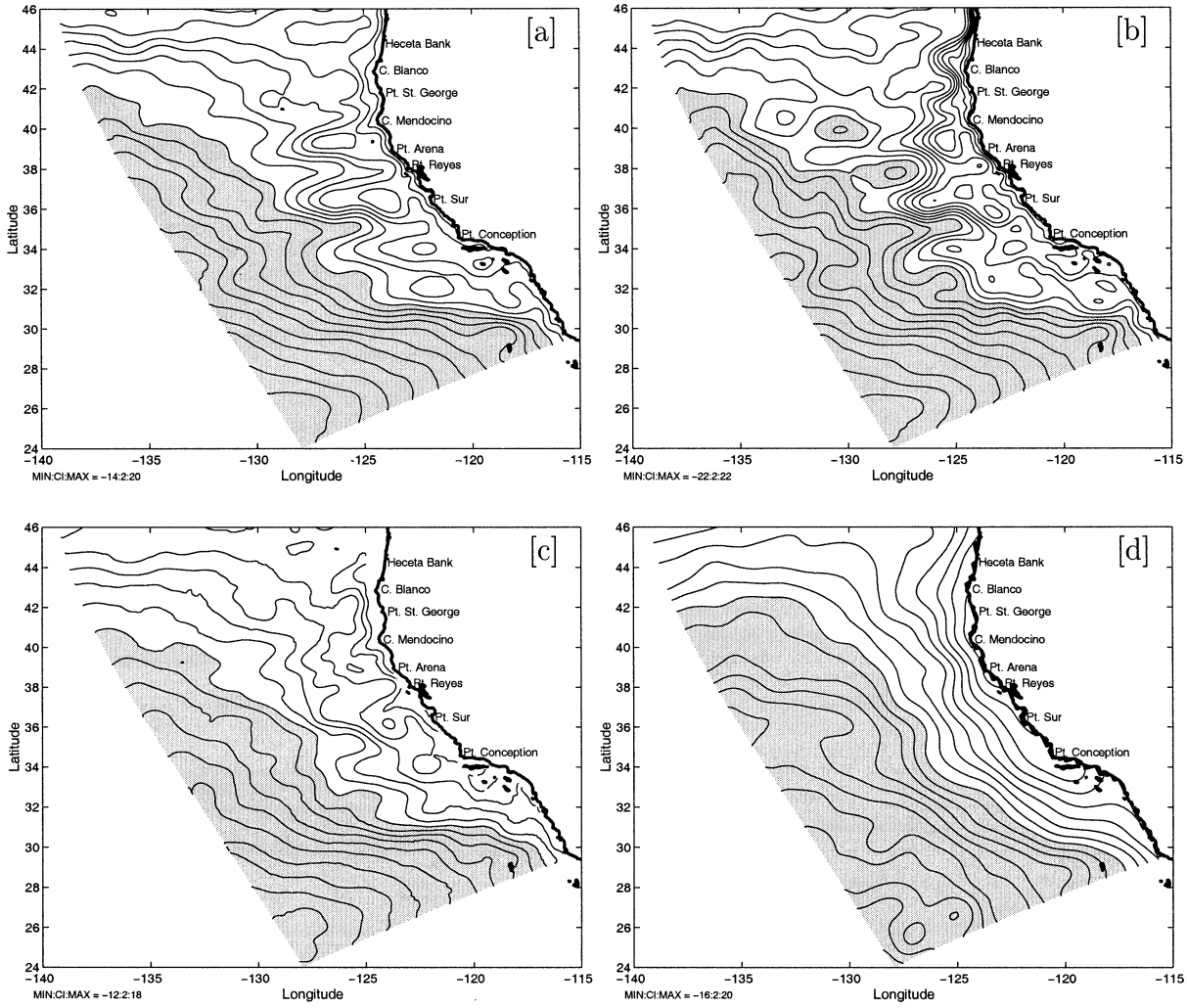

FIG. 6. Comparison of surface heights [contour interval (CI) = 2 cm], as observed and modeled (with 5-km resolution): (a) model, annual-mean SSH; (b) model, summer-mean SSH; (c) model, annual-mean, dynamic height relative to 500 m; and (d) Levitus et al. (1994), annual-mean, dynamic height relative to 500 m.

tween the nearshore and oceanic currents (poleward oceanic current), which abuts the CUC but has a distinct velocity maximum. Both these subsurface poleward currents lie close enough to the surface that one can expect transient surfacing events that might be interpreted as manifestations of the DC. McCreary et al. (1987) ascribed their poleward oceanic current to wind curl forcing, as the true dynamics of the DC. In this section [see also sections 4e(1) and 4e(2) for model sensitivities], we show that both wind curl and eddy vorticity fluxes are driving influences on this poleward flow.

In the cross-shore circulation, the strongest flow is the offshore Ekman currents in the shallow ($\sim$20 m) boundary layer, with a mean speeds of about 4 cm s^{-1}. In this surface layer the thermal stratification is stronger than the haline due to the importance of local surface heating, but in the pycnocline T and S contributions to stratification are comparable. The subsurface, onshore return flow spans several hundred meters throughout the pycnocline, and it is particularly strong over the continental slope. Interestingly, though, there is a local overturning circulation (e.g., at depth 300 m about 100 km offshore) in the opposite sense that crosses the deep poleward flow [section 4e(1)].

The CCS has primarily a baroclinic meridional circulation, but it has a weak barotropic component as well. Figure 20 (upper right) compares the simulated and Sverdrup alongshore transports in the upwelling region: the positive slope within about 200 km of the coast indicates a poleward barotropic flow (in the direction of the CUC) and the negative slope farther offshore an equatorward flow in the direction of the CC and the subtropical gyre. The model and Sverdrup transports are generally similar and weak (less than 1 Sv, where Sv $\equiv 10^6$ m^3 s^{-1}) though the model's flows are somewhat stronger throughout the CCS

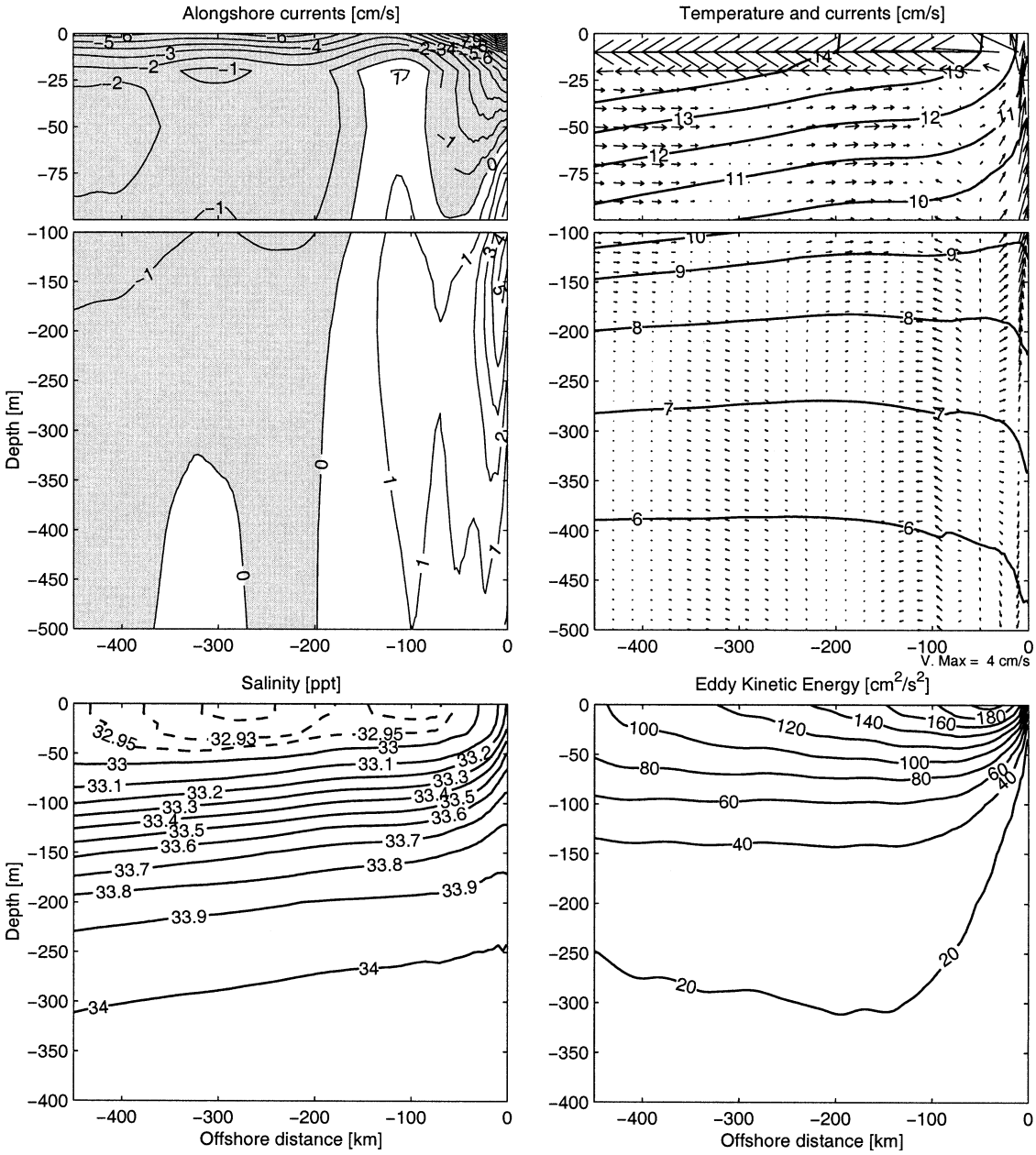

FIG. 7. Alongshore currents (top left), cross-shore currents (vectors top right), temperature (top right), salinity (bottom left), and EKE (bottom right) in the USWC upwelling region 34.5°–43°N from the model with 5-km resolution.

[consistently across resolution and wind forcing; section 4e(1)]. The inshore poleward flow is consistent with the idea of a DC driven by the wind curl (Munk 1950; McCreary et al. 1987). The weak transport results from compensating surface equatorward and subsurface poleward flows; in particular, the shelf and slope transports are quite small (Fig. 20 upper right; see 0–100 km).

The dynamics of alongshore transport can be examined in the time- and alongshore-averaged, depth-integrated momentum and vorticity balances. McCreary et al. (1991) examined the momentum balance and found, as we do, a small contribution from Reynolds stresses, compared to either surface Ekman balance or subsurface geostrophic balance. So they concluded that the effect of Reynolds stresses is weak, in contrast with the more significant eddy heat fluxes in the energy and heat balances [sections 4d(2) and 4d(3)]. However, the Reynolds stresses do account for significant departures in the alongshore transport from classical Sverdrup balance, and this is most readily seen in the time-mean vorticity balance:

$$\int_z \frac{\partial}{\partial t}\left(\frac{\partial \overline{v}}{\partial x} - \frac{\partial \overline{u}}{\partial y}\right) dz = -\int_z \beta \overline{v}\, dz + \mathrm{curl}_z[\overline{\tau_x^s}, \overline{\tau_y^s}] - \mathrm{curl}_z[\overline{\tau_x^b}, \overline{\tau_y^b}] - \int_z \mathrm{curl}_z\left[\frac{\partial(\overline{u^2})}{\partial x} + \frac{\partial(\overline{uv})}{\partial y}, \frac{\partial(\overline{v^2})}{\partial y} + \frac{\partial(\overline{uv})}{\partial x}\right] dz. \quad (3)$$

The left-side term represents the tendency, which is null in equilibrium; the right-side terms represent, respectively, planetary vorticity advection (BETA), wind stress curl (WIND), bottomstress curl, and vorticity advection (mean and eddy contributions are respectively termed ADVECTION and EDDY). The bottom stress makes only a weak contribution because the bottom flow is weak, and it will be henceforth ignored. Also, mean vorticity advection is small in comparison with eddy advection, as usual for a parallel flow (which ADVECTION is by definition). EDDY comprises the contributions from spatially fixed meanders about the alongshore-mean position of the currents (STANDING EDDY; cf. Fig. 6b) and from temporal variability (TRANSIENT EDDY). Figure 8 (top panel) shows the vorticity balance for the 5-km resolution case, averaged over the upwelling region and depth integrated over the top 1000 m (the results are qualitatively similar when integrated over the full depth). We see a nearly closed balance between WIND, BETA, and EDDY (TRANSIENT + STANDING). On a large cross-shore scale of hundreds of kilometers, WIND + BETA $\approx$ 0 (i.e., Sverdrup balance). At smaller scales the balance is affected by EDDY which appears as an offshore oscillation of wavelength ~200 km. Around 100 km from the coast EDDY induces positive vorticity resulting in increased poleward transport [as compared with lower-resolution cases in which both EDDY and the subsurface poleward flow are weaker; section 4e(2)], evident in Fig. 7 with its peak flow around depth 250 m. Farther offshore, around 200 km, EDDY changes sign and induces an equatorward transport (cf. Fig. 7). Figure 8 (bottom panel) shows that transient and standing eddy terms have comparable magnitudes but different cross-shore profiles.

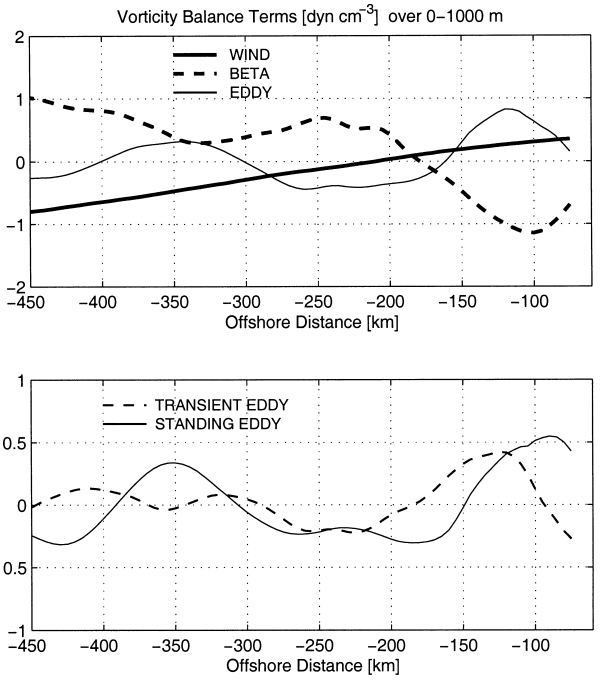

FIG. 8. Vorticity balance (dyn cm^{-3}) averaged over the upwelling region (34.5°–43°N) and depth-integrated over the top 1000 m. A smoothing operator was applied to eddy terms.

The alternating equatorward/poleward nature of mean alongshore currents in the CCS also appears in the CalCOFI estimation of geostrophic flows. Hickey (1979) discusses the mean flow of the CC based on CalCOFI data and hypothesizes that there are two distinct regions of strong southward flow separated by a region of reduced southward or even northward flow. Lynn and Simpson (1987) found no evidence of separate branches in the distributions of water characteristics. Therefore, they argue that eddy–current interaction could produce the appearance of branching of the CC in a long-term mean, producing a strengthening of the equatorward flow on one side of the eddies and weakening or reversal on the other side. This explanation is consistent with our results, which show that these alternating currents may be driven by both standing and transient eddies. Note that the poleward current has a weak baroclinic component as it flows in a region of strong eddy mixing which erodes the density slopes [see the temperature profile in Fig. 7 and discussion about eddy mixing in section 4d(3)]. Therefore it extends deeper than the adjacent equatorward flow and connects at depth with the CUC.

c. Seasonal currents

Both the seasonal wind forcing and current response are large in the CCS. Indeed, it is a valid interpretive question whether the CCS is more fundamentally driven by time-mean or quasiperiodically pulsed winds. The evolution of the seasonal-mean flow is driven by the seasonal winds plus widespread westward propagation. The area-integrated surface KE is largest in late summer (Fig. 1)—as is also observed with both drifters and al-

→

FIG. 9. Model (5-km resolution) and TOPEX/ERS mean-seasonal anomalies of SSH (CI = 2 cm). Winter is defined as the period from 15 Dec to 15 Mar, and the other seasons are the successive 3-month periods.

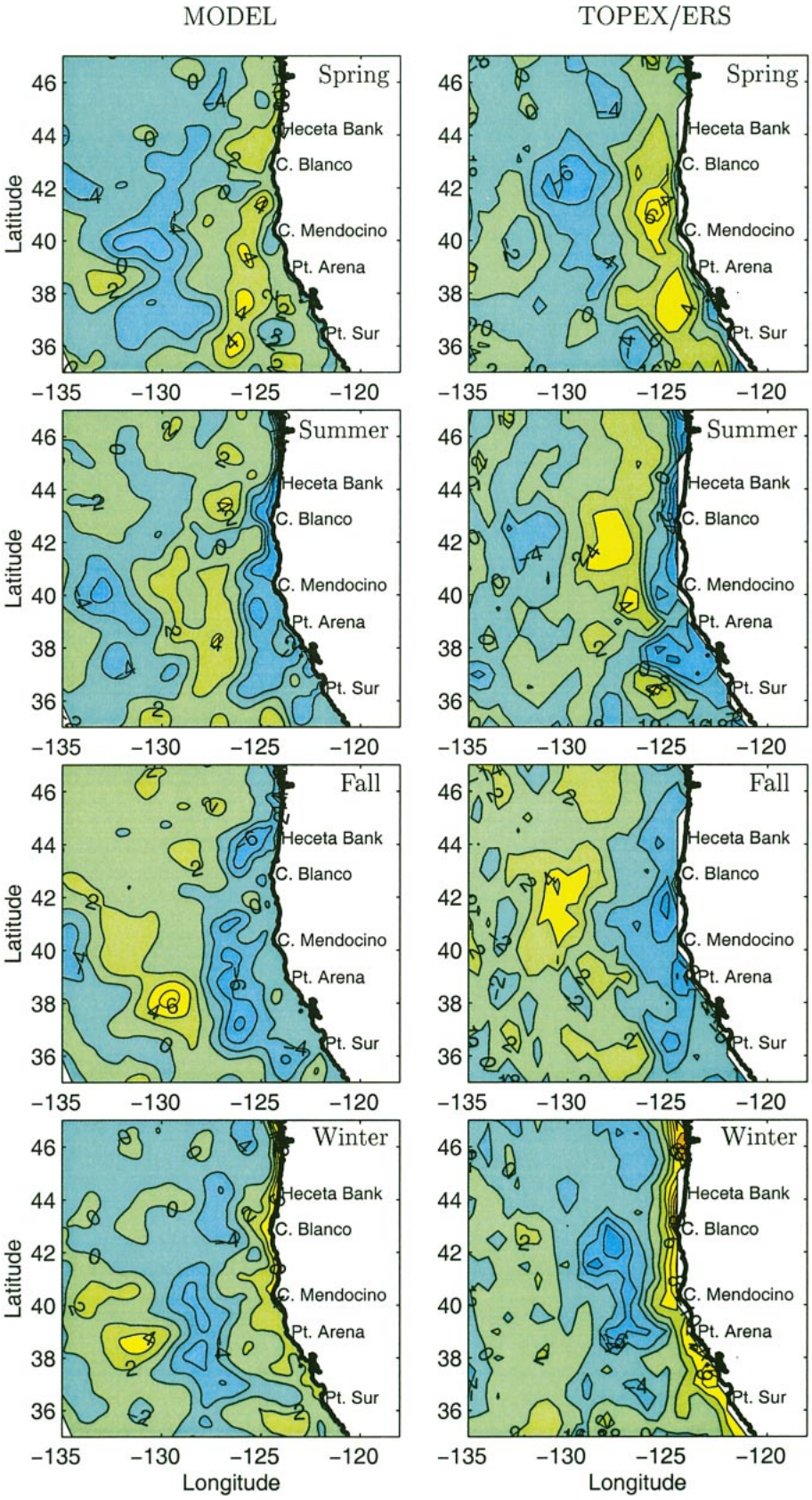
MODEL
TOPEX/ERS
Spring
Summer
Fall
Winter
Heceta Bank
C. Blanco
C. Mendocino
Pt. Arena
Pt. Sur
Latitude
Longitude
46
44
42
40
38
36
−135
−130
−125
−120

timetry (Kelly et al. 1998)—and it follows the strongest equatorward winds in the spring and summer.

Seasonal-mean SSH anomalies are shown in Fig. 9 for both the simulation and an analysis of TOPEX/ERS satellite altimetry (Strub and James 2000). The 6-yr ERS and TOPEX analysis was chosen here to combine high cross-track resolution from ERS (repeat cycle of 35 days and zonal separation of ~65 km at 40°N) and high temporal resolution from TOPEX (10-day repeat cycle and a zonal track separation of ~240 km at 40°N). TOPEX and ERS data were, respectively, collected during the periods 1994–99 and May 1995–99. The altimeter data along goundtracks were gridded on a 0.5° by 0.5° grid at approximately 15-day intervals using 35 days of data in a weighted successive correction scheme (Strub and James 2000). The simulated and observed SSH anomalies agree well in magnitude and are qualitatively similar in their patterns. A narrow, southward, surface current is generated near the coast in spring (where the SSH anomaly is low), in association with upwelling fronts. This current gets stronger and moves offshore in summer. By fall the low SSH anomaly is hundreds of kilometers offshore as the broad CC with poleward inshore currents. In winter and south of Cape Mendocino, inshore currents are weak and opposite to the wind direction, while along the coast of Oregon and Washington, a stronger, more continuous poleward current appears as the Aleutian low moves southward, associated with a high SSH anomaly at the coast.

However, the simulated and observed SSH anomalies are discrepant in pattern details on the smaller scale of ~100 km, some of whose extrema are relatively large. The area- and time-averaged correlation coefficient over the most eddy-energetic region (i.e., 34.5°–40°N, 0–700 km offshore) is only 0.47, although this correlation increases substantially over the comparable domain north of Cape Mendocino (i.e., 40°–46°N, 0–700 km offshore) where it is 0.68. In the northern region, with long stretches of nearly straight coastline, the nonseasonal EKE variability is relatively much smaller (sec. 4d), and the seasonal variability is larger with both upwelling and downwelling seasons. Some of the discrepancy, particularly in the southern region, may be due to aliasing of mesoscale and interannual variability in the limited altimetric record and model integration period (the sampling error is about 2 cm for both model and altimeter seasonal signals, which is on the order of the largest discrepancies), but some may be due to errors in the model's mean-seasonal wind forcing [section 4e(1)] or missing intraseasonal and interannual forcing (which may conceivably have an impact on the seasonal scales).

To filter out some of the small-scale, seasonal features, we make alongshore averages. Figure 10 shows summer–winter sea level changes for both model and altimetry over the region (34.5°–40°N, 0–700 km offshore). The largest seasonal changes occur in a 100-km-wide, nearshore zone and in the adjacent 300-km-wide, offshore zone. Nearshore and offshore seasonal changes are out of phase as a result of westward propagation of the near-shore signal generated at the coast (Fig. 12 below). In these filtered fields the model reproduces fairly well the seasonal cycle in phase and magnitude, although underestimating the amplitude at the nearshore and offshore extrema. For the nearshore region, the positive anomaly observed off central California in the winter season (an expression of the DC) is probably underestimated in the model because the COADS wind curl forcing is too weak; that is, the wind is too upwelling-favorable, particularly in winter [section 4d(1)]. Figure 11 illustrates the seasonal evolution of SSH anomalies over the nearshore zone of both northern and southern regions in comparison with the alongshore wind stress. The peak wind-driven upwelling season is in summer in the northern region but earlier in spring off California (consistent with observations; e.g., Strub and James 2000). Both model and altimeter data show near simultaneity of winds and oceanic response, suggesting that the coastal seasonal cycle is locally forced, with no evident oceanic teleconnection between southern and northern regions.

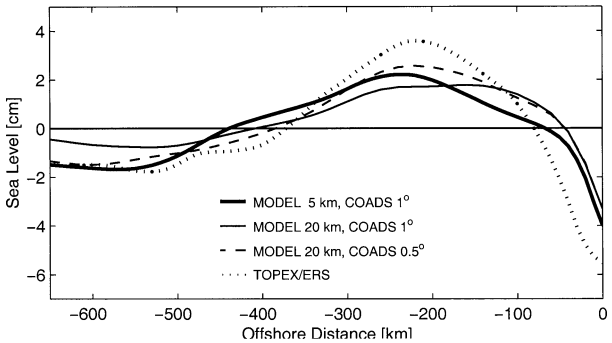

FIG. 10. Model and TOPEX/ERS seasonal differences (summer–winter) of mean-seasonal SSH anomalies averaged over an alongshore coordinate between 34.5° and 46°N. Three model solutions are presented with different resolutions and winds. Winter is defined here as the period from 15 Sep to 15 Mar, and summer is the successive 6-month period.

The seasonal westward propagation in the upwelling region of CCS is demonstrated in Fig. 12, both for SSH (left panel) and for surface and depth-integrated EKE. Extrema in all these quantities move offshore at a speed of about 2 cm s^{-1} in quasi-recurrent seasonal patterns. This speed is about what is expected from baroclinic Rossby waves, as also has been pointed out in observational analyses (Chelton and Schlax 1996; Kelly et al. 1998). However, it is noteworthy that the propagating signal appears in the model more as propagating eddies (Figs. 2–5) rather than as wavefronts.

d. Mesoscale variability

1) VARIANCES

The standard deviation of SSH is compared in Fig. 13 (upper panels) for the model and TOPEX/ERS altimetry (data processing described in section 4c). In both cases there is a band of offshore maxima along the path

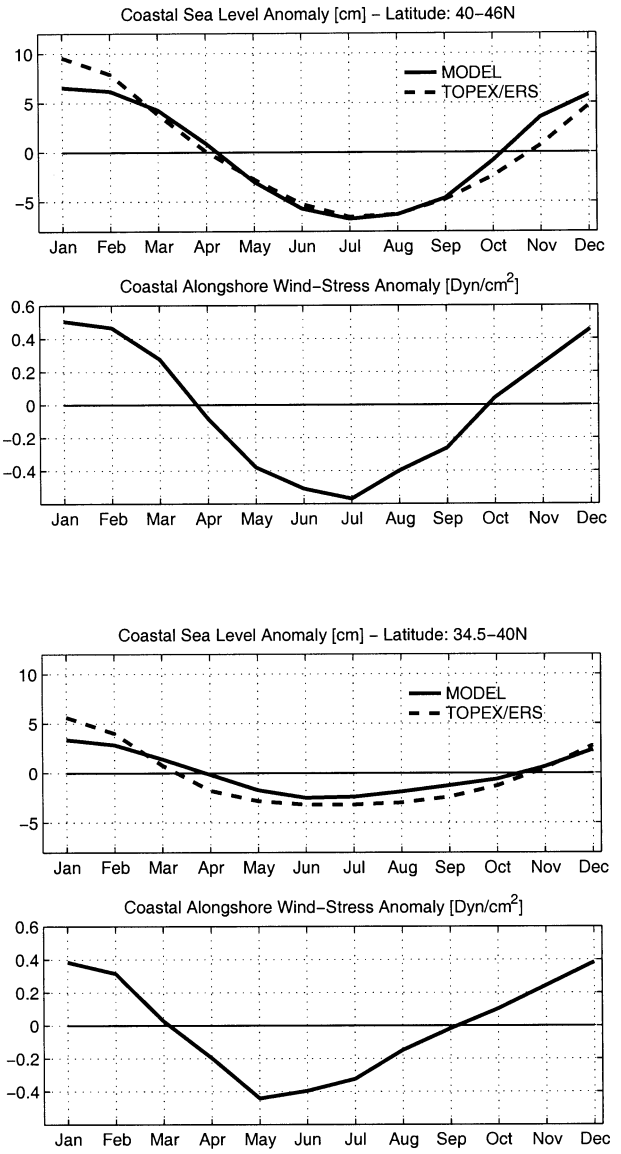

FIG. 11. Nearshore seasonal cycle of simulated and TOPEX/ERS SSH anomalies and alongshore wind stress. The variables are averaged over 100-km-wide alongshore strips (top) between 40° and 46°N and (bottom) between 34.5° and 40°N.

of the offshore CC approximately 300 km from shore all along the USWC. The largest values occur in the upwelling region between 36° and 40°N. A noticeable difference occurs in the magnitude of the SSH variability: the model seems to underestimate local maxima by about 20%–30%. This difference is much lower when compared with the ERS analysis alone (not shown); TOPEX has higher variability. But there is a good match in the positions of local maxima and minima along the band of high values, suggesting that the eddy flow is partly controlled by alongshore topographic variations. In addition there are extrema around capes that are underestimated in the model, likely for similar reasons as for the seasonal SSH (i.e., forced synoptic and interannual variability in nature; wind errors in the model's forcing).

Figure 13 (lower right) shows a surface EKE analysis of drifter measurements on a grid 5° × 5° (Swenson and Niiler 1996). The drifter data were obtained in five experiments that deployed satellite-tracked drifting buoys in the California Current System during late spring to early fall in 1985–88. Since these data are mostly representative of the summer season, we compare it with the model's mean-summer surface EKE (lower left). We have smoothed the model field to facilitate the comparison with the low-resolution drifter analysis, but not by as much as the drifters. Both surface EKE fields show a triangular shape with a maximum near Point Arena, although EKE values in the model are more aligned alongshore (the drifter data is averaged zonally in rather large bins). Maximum values are about 500 $cm^2\ s^{-2}$ in both cases, and as opposed to SSH variability the maxima are located near the coast. On the other hand, because they are repelled by surface divergence, drifters undersample coastal upwelling, which may partly be why the nearshore discrepancies seen in the SSH comparisons are not evident here.

An integrated comparison over the most energetic region (33°–40.5°N, 124°–132°W, but excluding a boundary strip of width ~50 km, hereinafter K98) can also be made with a compilation of surface EKE from altimeter and drifter data by Kelly et al. (1998) (Table 1). The mean surface EKE values are 122, 150, and 180 $cm^2\ s^{-2}$ for respectively the simulation, altimetry, and drifters. Kelly et al. suggest that the difference between drifters and altimetry are due to the ageostrophic velocity not calculable from altimetric SSH measurements. The simulated mean EKE is somewhat smaller than the observed, and a similar remark can be made about the seasonal variations between the summer peak and winter low (Table 1). We suggest that the model is simulating rather well the observed eddy variability, considering that its forcing lacks synoptic and interannual contributions and that its dependence on resolution has not yet converged [section 4e(2)]. From this we conclude that the principal cause of EKE in the CCS is intrinsic instability rather than forced response.

Local maxima in the mean surface EKE (Fig. 14a)

TABLE 1. Time-mean, surface EKE ($cm^2\ s^{-2}$) over the K98 domain (33°–40.5°N, 124°–132°W, excluding a boundary strip).

EKE ($cm^2\ s^{-2}$)	Model (20-km resolution)	Model (10-km resolution)	Model (5-km resolution)	Altimeter	Drifters
Annual	37	68	122	150	180
Seasonal difference	14	25	57	100	

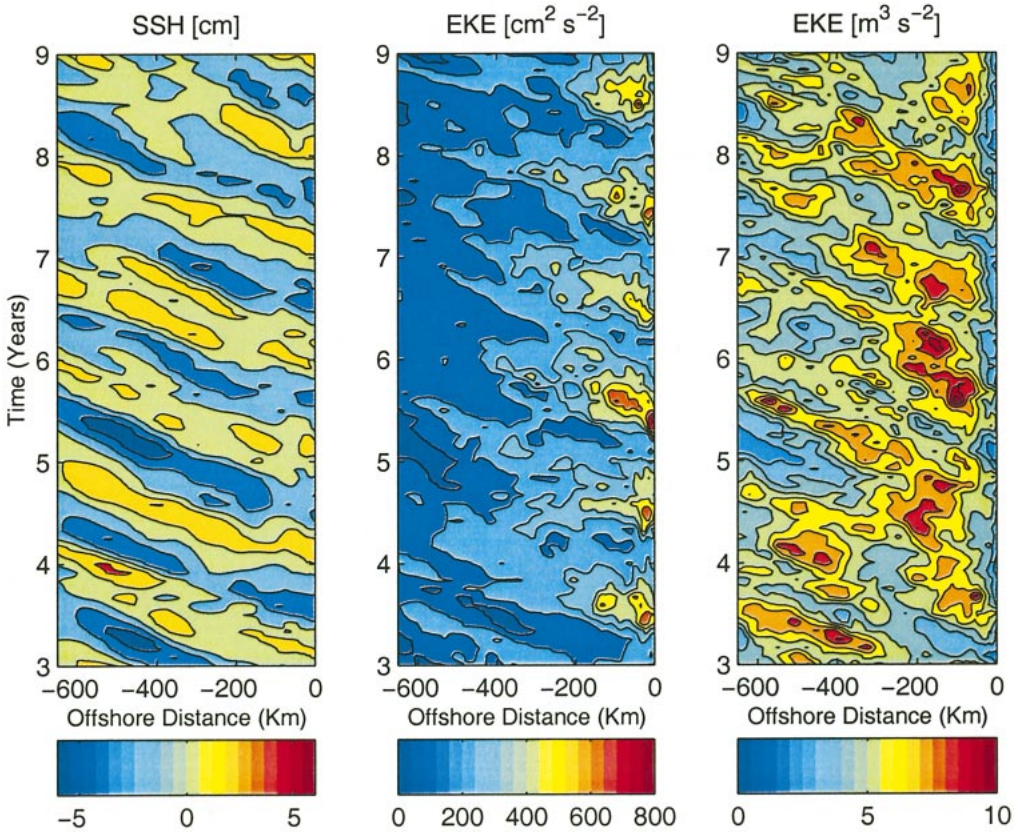

FIG. 12. Hovmoeller plots for SSH anomalies (CI = 2 cm), surface EKE (CI = 100 cm^2 s^{-2}), and depth-integrated EKE (CI = 1 m^3 s^{-2}) from the model with 5-km resolution and averaged alongshore in the upwelling region (34.5°–43°N).

occur near Cape Blanco, Cape Mendocino, Point Arena, Point Reyes, Point Sur, and Point Conception, demonstrating the expected strong influence by capes and ridges [explored further in section 4e(3)]. (The same is true for the summer EKE but this is blurred by the smoothing used in Fig. 13). We decompose surface EKE into separate contributions from seasonal and nonseasonal and from geostrophic and ageostrophic currents (Figs. 14b–d). The seasonal and ageostrophic EKE calculated as the differences between total and, respectively, nonseasonal and geostrophic EKE. The geostrophic component is calculated using geostrophic velocities derived from the model SSH:

$$u = -\frac{g}{f}\frac{\partial \eta}{\partial y}, \qquad v = \frac{g}{f}\frac{\partial \eta}{\partial x}. \tag{4}$$

These relations are commonly used to estimate eddy energy from satellite altimetry; therefore, our model analysis of geostrophic EKE is more directly comparable to satellite estimates. Figure 14 shows that the bulk of the EKE is nonseasonal and geostrophic. The largest seasonal EKE is found along the coasts of Oregon and Washington, where seasonal winds drive a seasonal, ageostrophic Ekman drift and its associated alongshore currents. Off California there is only weak energy at the seasonal frequency. About 20% of the total EKE on the California shelf and slope is due to ageostrophic currents (which by definition are undetected by SSH measurements). Their strong nearshore confinement indicates that they are not primarily Ekman currents (which have only seasonal variability in our simulations, with a relatively small surface variance of about 10 cm^2 s^{-2}), but rather are a consequence of significant nonlinear advection of momentum in the upwelling dynamics.

The seasonal propagation in EKE (Fig. 12) starts from a burst of nearshore, near-surface instability in the upwelling season that progressively moves offshore and downward into a large reservoir of the offshore, subsurface eddy field with a long dissipation time—as demonstrated by the much longer offshore decay scale of depth-integrated EKE compared to surface EKE (cf. Fig. 1). The seasonal alongshore currents move synchronously with the EKE, indicative of seasonally modulated, mean-eddy dynamical coupling [sections 4c(2), 4c(3)]. An offshore and downward fan of annual mean EKE is also evident in Fig. 7d. Depth-integrated values of EKE from these profiles show a constant level of energy from the coast up to 200 km offshore, and then a slow decrease far-

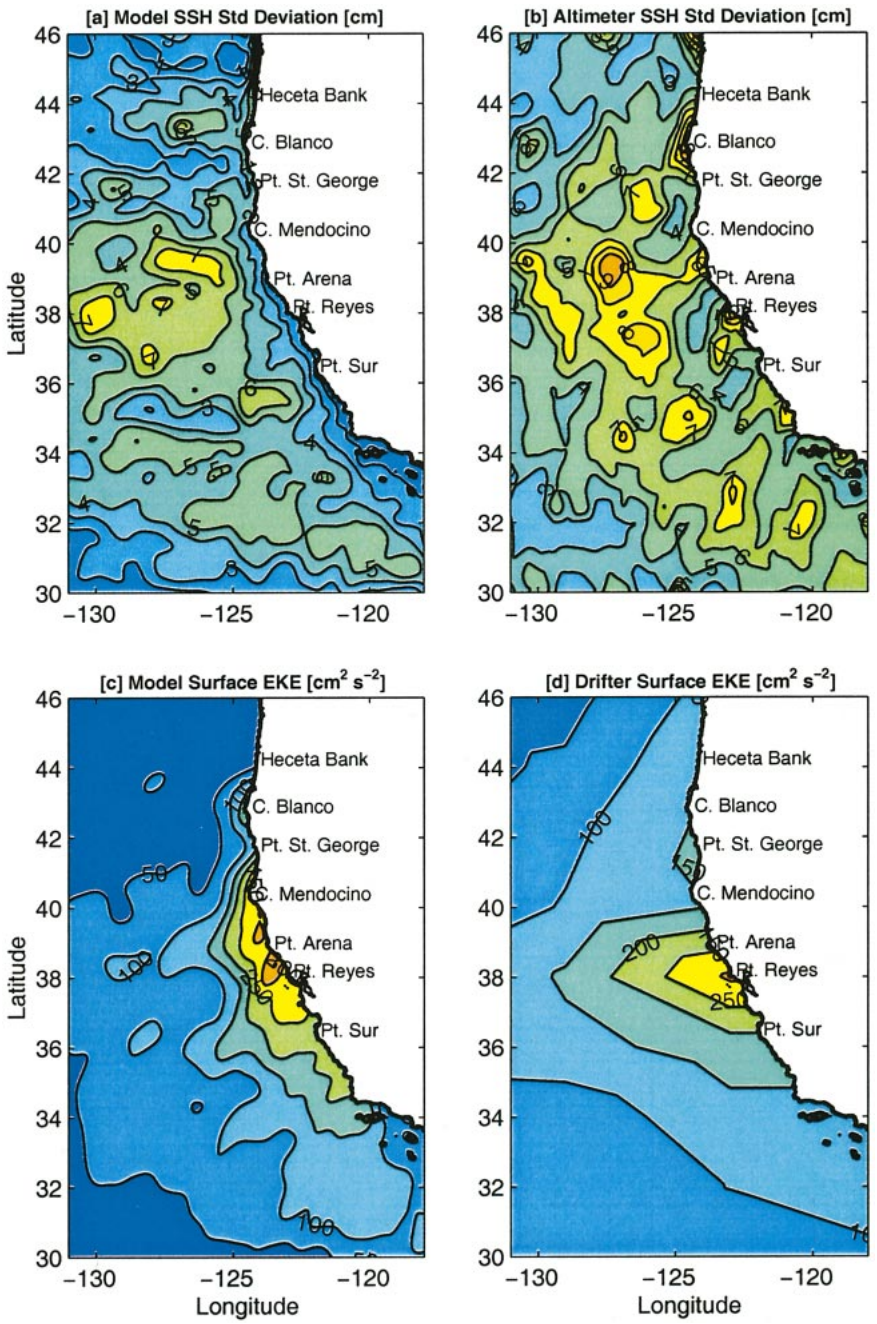

FIG. 13. Comparison of SSH standard deviation (CI = 1 cm) and mean-summer, surface EKE (CI = 50 cm^2 s^{-2}), as observed and modeled (with 5-km resolution). (TOPEX/ERS altimeter SSH standard deviation was provided by T. Strub, and drifter surface EKE by P. Niiler.)

ther offshore. As a result, the offshore integrated EKE at 500 km is only 15% lower than its nearshore value. By comparison, the mean surface EKE is 50% lower, decreasing offshore in a more abrupt and systematic way. Earlier studies have attributed the decay of the surface EKE signal in the coastal transition zone to damping by vertical mixing (Kelly et al. 1998; McCreary et al. 1991). Haney et al. (2001) suggest an alternative mechanism without significant damping: namely, the EKE generated during the upwelling season from baroclinic instabilities may also spread downward via a transformation into more barotropic currents. With a quasigeostrophic CCS model, Ikeda et al. (1984) similarly show that the growth of disturbances in the CC follows an inverse cascade, including to larger vertical scales, due to nonlinear in-

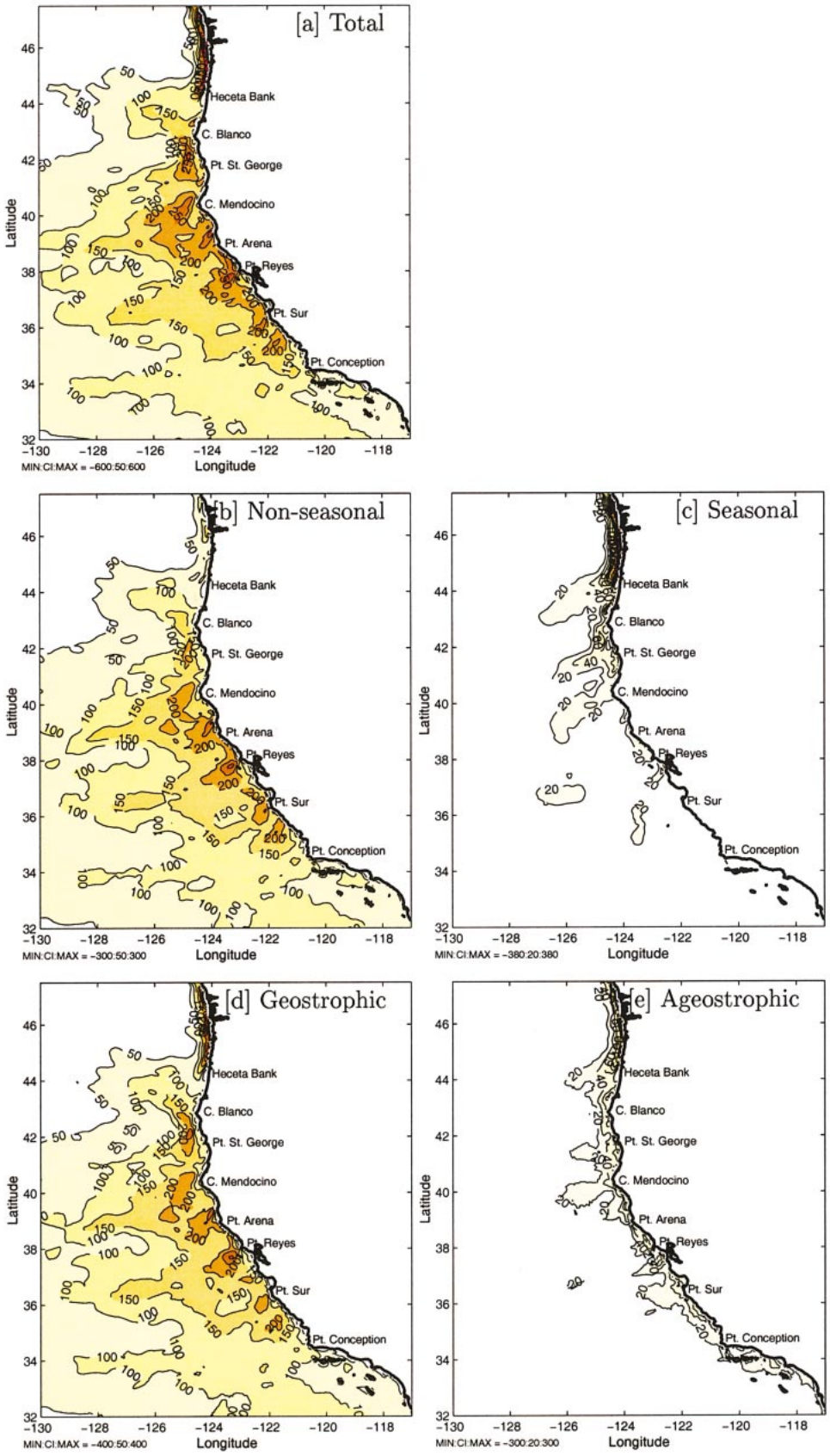
[a] Total
[b] Non-seasonal
[c] Seasonal
[d] Geostrophic
[e] Ageostrophic
Heceta Bank
C. Blanco
Pt. St. George
C. Mendocino
Pt. Arena
Pt. Reyes
Pt. Sur
Pt. Conception
Latitude
Longitude
MIN:CI:MAX = -600:50:600
MIN:CI:MAX = -300:50:300
MIN:CI:MAX = -380:20:380
MIN:CI:MAX = -400:50:400
MIN:CI:MAX = -300:20:300

teractions. This is, of course, a generic behavior of geostrophic turbulence (Charney 1971; Rhines 1979; McWilliams et al. 1994), and the CCS appears to be a particular manifestation. Our simulations support these latter interpretations.

2) Energy conversion and instability

Energy budgets are useful in quantifying the relative importance of instability and eddy-mean interaction mechanisms. Volume-integrated energy budget equations can be derived for mean and eddy KE (K_m, K_e) and mean and eddy available potential energy (P_m, P_e), which contain surface wind and buoyancy forcing terms F, spatial transport terms T, dissipation terms D, and conversions among the energy types, namely, mean-to-eddy barotropic conversion K_mK_e and baroclinic conversion on the path through K_mP_m, P_mP_e, and finally P_eK_e (Harrison and Robinson 1978). Integrated over a closed basin, the T vanishes, which clearly distinguishes them from the conversion terms; however, when the domain of integration is open and transport terms are nonzero, some of the conversion terms are more difficult to interpret. Here we focus on the wind work (F_mK_m and F_eK_e) and barotropic and baroclinic conversions (K_mK_e and P_eK_e) relevant to EKE generation in the model:

$$F_mK_m = \frac{1}{\rho_0}(\overline{u\tau_x} + \overline{v\tau_y}) \tag{5}$$

$$F_eK_e = \frac{1}{\rho_0}(\overline{u'\tau'_x} + \overline{v'\tau'_y}) \tag{6}$$

$$K_mK_e = -\left(\overline{u'u'}\frac{\partial\overline{u}}{\partial x} + \overline{u'v'}\frac{\partial\overline{u}}{\partial y} + \overline{u'w'}\frac{\partial\overline{u}}{\partial z} + \overline{v'u'}\frac{\partial\overline{v}}{\partial x} + \overline{v'v'}\frac{\partial\overline{v}}{\partial y} + \overline{v'w'}\frac{\partial\overline{v}}{\partial z}\right) \tag{7}$$

$$P_eK_e = -\frac{g}{\rho_0}\overline{\rho'w'}. \tag{8}$$

We denote the zonal and meridional components of the wind stress by (τ_x, τ_y) and the time-mean of any quantity ϕ and its perturbation by ($\overline{\phi}$, ϕ'). The result integrated over the upwelling region (34.5°–43°N, 500 km offshore) is shown in Fig. 15. The large input of energy from the wind to the mean field mostly fluxes through the open boundaries (presumably mostly to the west by Rossby wave processes), and most of the rest (about 20%) is spread between barotropic and baroclinic conversions. The latter conversion is dominant by a factor of 2, consistent with the dominance of baroclinic instability. Figure 15 (right panel) shows a cross-shore profile of the conversion terms averaged over 50-km subdomains. Here again we see distinctive inshore and offshore regimes. The maximum conversion occurs within 150 km of the coast, particularly for the barotropic conversion presumably due to the strong lateral shears in the coastal jet and CUC. Offshore there is a sustained baroclinic conversion across the whole CC, while barotropic conversion is much weaker. Note that the relatively low value of baroclinic conversion very near the coast (top, right panel) is an artifact of upwelling and downwelling associated with the strong seasonal cycle north of Cape Mendocino. Indeed, this seasonal signal is characterized by an energy pathway of the type F_eK_e then K_eP_e (colder subsurface water going up in summer and warmer surface water going down in winter). As a result, seasonal K_eP_e is strongly negative and may lead to an underestimation of the mesoscale baroclinic conversion P_eK_e which is positive. Therefore, a better estimation of baroclinic instability is done by extracting the seasonal signal from the solution, then computing the conversion terms (Fig. 15, bottom right panel).

Our analysis is largely consistent with that of Auad et al. (1991) for their quasigeostrophic solution. In a more complete energy budget analysis, they found that the wind increases the mean KE (F_mK_m), which is fluxed through the open boundaries because of Rossby wave processes and also converted into potential energy (K_mP_m). The latter is then converted into eddy potential energy (P_mP_e) and subsequently into EKE (P_eK_e) through baroclinic instability. Their analyses show little barotropic conversion (K_mK_e), which may be attributed to the limitations of quasigeostrophic approximations in frontal formation and the associated strong horizontal shears. An offshore increase in the eddy scale is consistently observed in laboratory experiments [see McCreary et al. (1991) for a review]. This is attributed to nearshore shear instability (often referred to as a Kelvin–Helmholtz instability) and a subsequent offshore dominance of larger-scale, baroclinic instability. We see this shear instability in the nearshore barotropic conversion (K_mK_e) and in the corresponding observation of cyclonic roll-up patterns (of the Kelvin–Helmholtz type) early in the upwelling season before the full development of squirts and eddies.

3) Eddy heat flux

The eddies interact with the mean flow through eddy heat and salt fluxes. We can write an equation for the time-mean T, here averaged in the vertical direction to the bottom:

←

FIG. 14. Model annual-mean surface EKE ($cm^2\ s^{-2}$) from the model with 5-km resolution: (a) total, (b) nonseasonal, (c) geostrophic, (d) seasonal, and (e) ageostrophic. Definitions are given in the text.

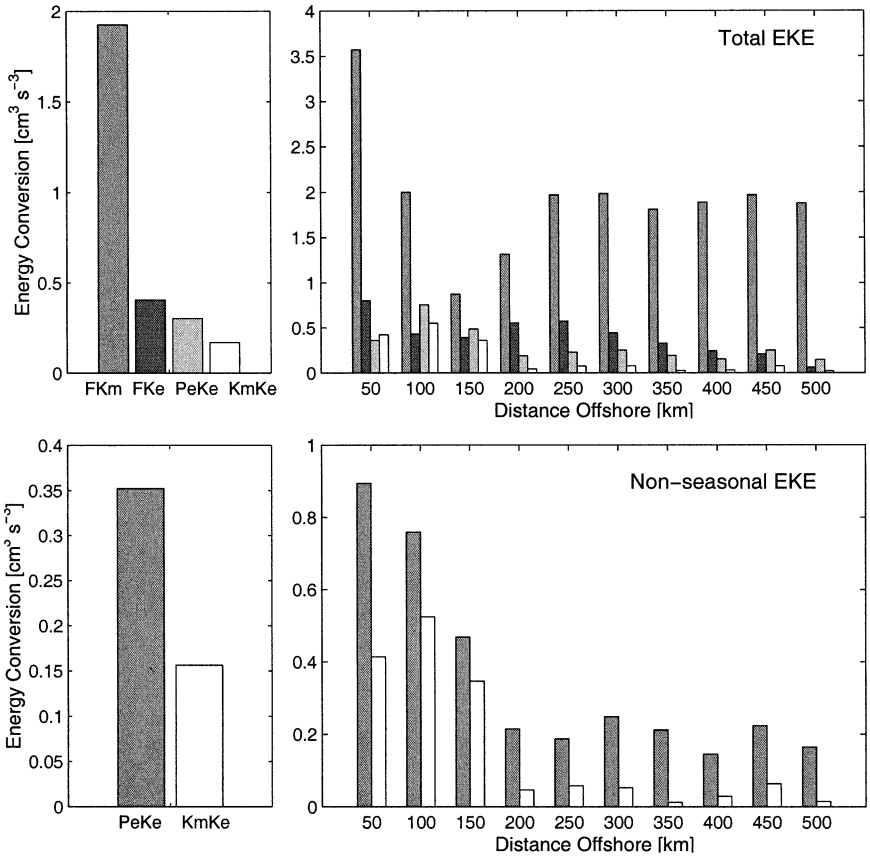

FIG. 15. Depth-integrated energy-budget components (cm^3 s^{-3}) from the model with 5-km resolution: (left) wind work (F_mK_m and F_eK_e) and barotropic/baroclinic conversion terms (K_mK_e and P_eK_e) for the upwelling region (34.5°–43°N, 500 km offshore); (right) cross-shore profile of the conversion terms averaged over 50-km intervals; (bottom) Same as top panels but for non-seasonal EKE conversion terms. In this case, the term F_eK_e is null.

$$\int_z \left(\frac{\partial \overline{T}\,\overline{u}}{\partial x} + \frac{\partial \overline{T}\,\overline{v}}{\partial y} \right) dz + \int_z \left(\frac{\partial \overline{T'u'}}{\partial x} + \frac{\partial \overline{T'v'}}{\partial y} \right) dz + \int_z [Q(\overline{T}) + D(\overline{T})]\, dz = 0. \quad (9)$$

This shows a balance between advective heat transport by the mean flow; heat transport by the eddies; surface heat flux Q; and parameterized, vertical and horizontal subgrid-scale mixing of heat D. We will focus on the transport by eddy flow, that is, a divergence of lateral eddy fluxes $\overline{T'u'}$ and $\overline{T'v'}$. In analogy with molecular transport, this is often written as functions of the gradients of $\overline{T}$,

$$\overline{T'u'} = -K_x \frac{\partial \overline{T}}{\partial x}, \qquad \overline{T'v'} = -K_y \frac{\partial \overline{T}}{\partial y}, \quad (10)$$

where K_x and K_y are cross-shore and offshore eddy diffusivities representative of the explicitly resolved eddy fluxes in the model. In this section we use these relations for the simulations and compare with the K estimates by Swenson and Niiler (1996), who used a set of drifting buoy trajectories in the CCS during 1985–88. They show that these flux/gradient relations do not always yield well-behaved eddy diffusivities; however, they are able to make estimations with sufficient confidence for some areas.

For our simulations we find that, by using only non-seasonal eddy contributions to the flux and excluding places with very low gradient of $\overline{T}$ in the computation of the diffusivities, a coherent and meaningful pattern emerges in the upwelling region (Fig. 16) except far offshore where some negative values occur. The cross-shore diffusivity K_x has maxima 100–200 km offshore with peak values off all the major headlands along the coast. The peak values are well correlated to the maximum offshore extension of standing-eddy meanders (cf. Fig. 6; standing eddies are also evident in the mean temperature field on Fig. 16), and they are located in a low-gradient band in $\overline{T}$ between the sharp coastal gradients and the larger offshore gradients in the CC. The alongshore diffusivity K_y is more uniform than K_x (not shown). In the region 33°–41°N, 127°–119°W, the average values are $K_x = 2.3 \times 10^3$ m^2 s^{-1} and $K_y = 1.3 \times 10^3$ m^2 s^{-1}; these are consistent with the estimates

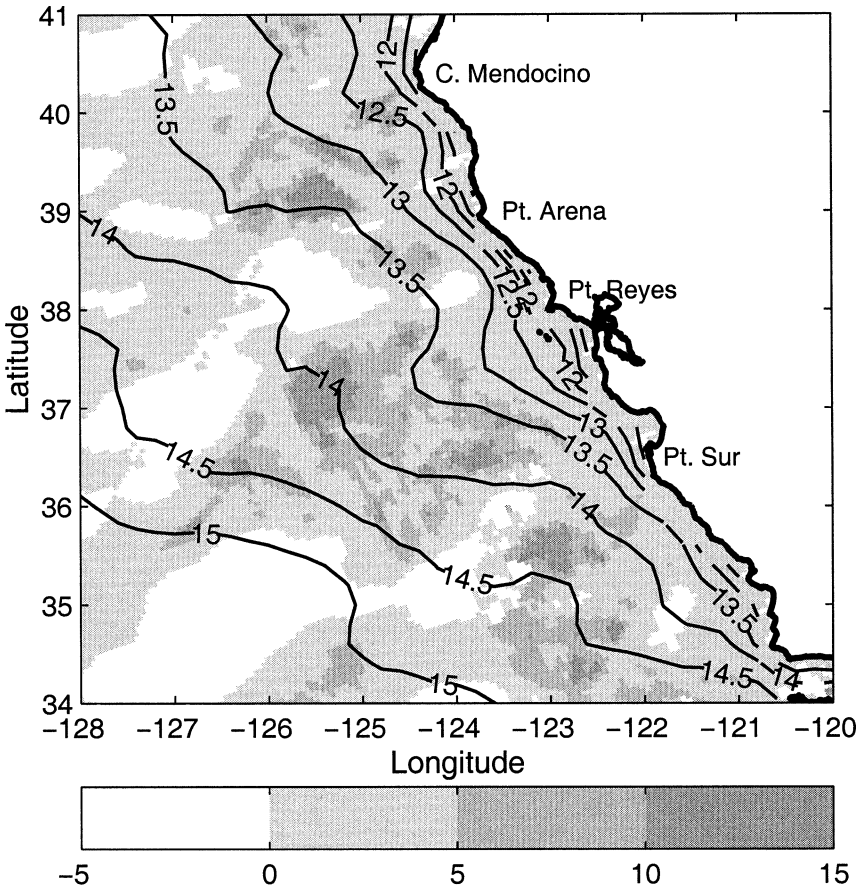

FIG. 16. Cross-shore eddy diffusivity for heat (10^2 m^2 s^{-1}; grayscale) superimposed on $\overline{T}(0)$ (CI = 0.5 K), from the model with 5-km resolution.

by Swenson and Niiler, namely, 1.1–4.6 × 10^3 m^2 s^{-1} with higher values for K_x.

We calculate diagnostically the mean and eddy heat flux and surface flux divergences in (9) using 3-day average fields (Fig. 17). Positive (negative) values for each term indicate a tendency to induce local warming (cooling). We see that large values occur primarily in the nearshore region. Typically the nearshore waters are cooled by the mean upwelling flow and warmed by both the eddy flux and the surface heat flux. The alongshore variations in the mean and eddy contributions are reminiscent of the alongshore variations in $\nabla\overline{\eta}$ (Fig. 6a) and EKE (Fig. 14a), respectively.

Table 2 lists the balance of terms in the heat budget for different locations. In all cases the residual contribution is rather small; it includes subgrid-scale diffusion (done implicitly by the upstream-differenced advection), eddy flux by resolved fluctuations on timescales shorter than 3 days, and the tendency term that is zero in equilibrium. Here we have concentrated our analysis on the region 36°–40°N, which has upwelling conditions all year long. Therefore, the results are more strictly representative of the upwelling regime, and the interpretation of the different terms in the budget is facilitated. We see distinctive behavior in the nearshore and offshore regions. Within 150 km from the coast and particularly within 50 km, the water is typically cooled by the mean offshore flux. Point Reyes and other headlands are locations of peak transport values. The offshore component is nearly compensated by the alongshore mean flux, and their sum is often more than an order of magnitude weaker than the components. A similar but weaker compensation occurs in the eddy flux: warming is caused by the offshore component, partly compensated by cooling from the alongshore component. The warming by surface heat flux is smaller at the nearshore locations than the transport terms but of the same order of magnitude. In the offshore regime, the water is cooled by both mean and eddy flow, and warmed by the surface flux. The components of the mean heat flux divergence have opposite signs with respect to their respective counterparts in the nearshore region. This indicates that offshore cooling is due to the southeastward path of the CC, with an alongshore component carrying colder water from the north but a shoreward component carrying relatively warm North Pacific Central Water, compensating for the cooling

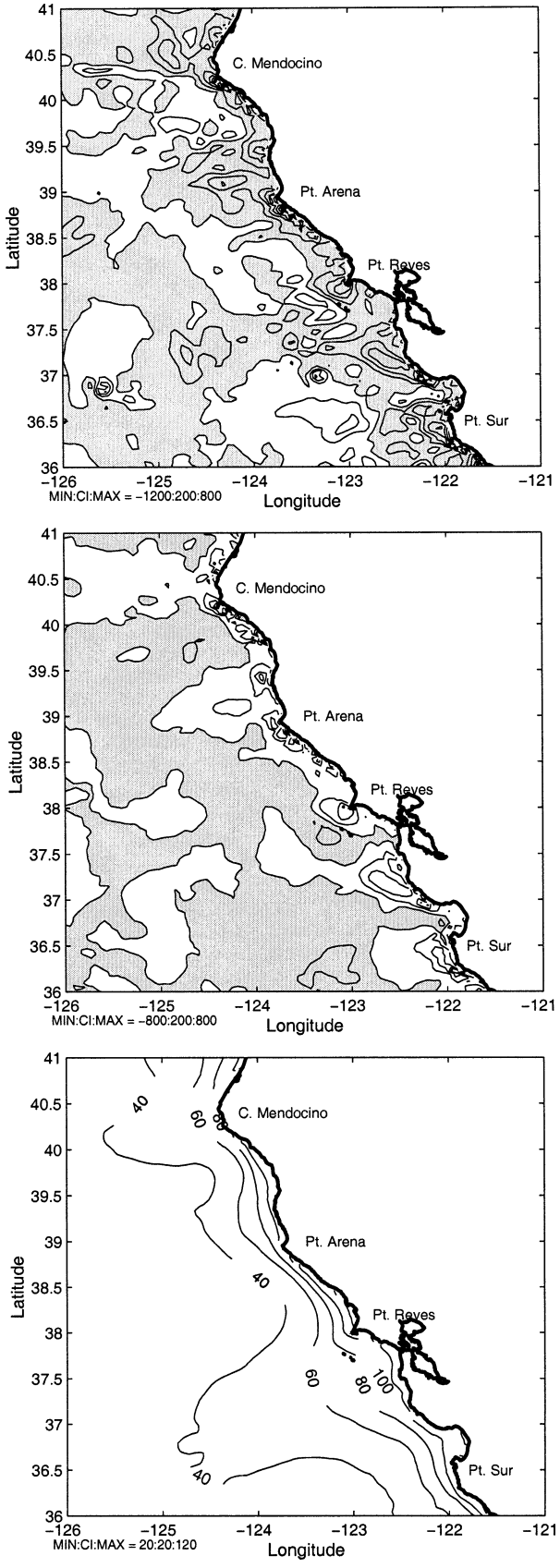

by Ekman transport (Fig. 7b). Contrarily in the nearshore region, the dominant subsurface mean currents are poleward, with a deep poleward current between 50 and 150 km from the coast and the CUC (Fig. 7a). Therefore, the water is warmed by subsurface alongshore currents but cooled by the offshore Ekman surface drift. The eddy heat flux divergence also has opposite signs in nearshore and offshore regions. This result can be explained by considering the eddy flux working as eddy diffusion. This eddy diffusion mixes cold nearshore water, originating from upwelling of subsurface water or equatorward flowing Pacific Subarctic Water, and warm offshore water fed by North Pacific Central Water. The result is a warming of coastal waters and a cooling of offshore waters. Even though the eddy fluxes are acting diffusively in their heat flux, they do coexist with both sharp coastal gradients and significant offshore gradients in SST. The large-area heat budget (i.e., averaged over a 500 km cross-shore extent, Table 2) is approximately consistent with the empirical estimates by Swenson and Niiler (1996): they show a smaller eddy and mean heat flux divergence—2–6 and 20 W m^{-2}, respectively, estimated from surface drifters and extrapolated over depth 50 m—as compared with the simulated values of 6 and 43 W m^{-2} integrated over the full depth. Our view of the CCS heat balances is also consistent with the 2½-layer numerical model of McCreary et al. (1991).

e. Model sensitivities

1) WIND

Wind analyses used to force oceanic models are available from in situ observations, remote sensing, and numerical weather prediction models with data assimilation. A comparison of available analyses has recently been conducted for the global ocean by the Joint WCRP/SCOR Working Group on Air–Sea Fluxes (Taylor 2000), and Bakun and Nelson (1991), and Enriquez and Friehe (1995) have more specially discussed the problems in local wind analyses along the USWC. The quality of wind data is particularly important at an eastern boundary where the distinction needs to be made between equatorward currents driven by alongshore equatorward wind and poleward currents driven by positive wind curl and where the orographic influences of coastal mountains and capes is substantial (e.g., direct wind stress measurements from a research aircraft around Point Arena show values that can be

←

FIG. 17. Equilibrium, depth-integrated heat balance (W m^{-2}) in the center of upwelling region from the model with 5-km resolution: (top) mean horizontal heat-flux convergence (CI = 200), (middle) eddy horizontal heat-flux convergence (CI = 200), and (bottom) surface vertical heat flux (CI = 20).

TABLE 2. Area-averaged components of the heat budget, $\rho C_p \dot{T}$ ($W\ m^{-2}$), at a point off Point Reyes and averaged over alongshore strips between 36° and 40°N.

Location area	$-\int_z \left(\frac{\partial \overline{T}\,\overline{u}}{\partial x} + \frac{\partial \overline{T}\,\overline{v}}{\partial y} \right) dz$	$-\int_z \left(\frac{\partial \overline{T'u'}}{\partial x} + \frac{\partial \overline{T'v'}}{\partial y} \right) dz$	Q	Residual
38°N, 123°W (Point Reyes)	−22 183 + 21 576 = −522	496 − 66 = 430	85	−6
36°–40°N Coast–50 km	−1952 + 1699 = −253	231 − 94 = 137	103	−13
36°–40°N Coast–150 km	−739 + 628 = −111	42 + 3 = 45	68	−2
36°–40°N 150–500 km	784 − 809 = −25	−15 − 4 = −19	30	−14
36°–40°N 0–500 km	470 − 513 = −43	−3 − 3 = −6	38	−11

more than five times as large as those obtained from long-term ship measurements using bulk aerodynamic formulas; Enriquez and Friehe 1995). From these sources we must be quite cautious about the reliability of the model forcing.

In the present study, we assess the potential model errors by analyzing the solution sensitivity to the wind forcing by comparing a few different datasets, although this issue warrants even more extensive investigation. We make the comparison with a coarse model resolution of 20 km for economy. Our standard forcing analysis, UWM/COADS with 1° spatial resolution (i.e., revised COADS from da Silva et al. 1994), is the one most widely used by oceanic modelers, because it has been the only global analysis extending over multiple decades. We compare the results to a solution with the 1° National Centers for Environmental Prediction (NCEP) operational analyses of surface winds (Parrish and Derber 1992), which uses various observations from surface marine measurements to *ERS-2* scatterometry. A third analysis used here is 0.5°-resolution UWM/COADS that is yet poorly documented and validated. Figure 18 shows annual-mean wind stress and associated Sverdrup streamfunction ψ_{sv} for the upwelling region ($\beta(\partial\psi_{sv}/\partial x) = \mathrm{curl}_z \tau_y$). The great smoothness in all the analyses is evident; for example, in COADS-1° only wavelengths greater than about 770 km remain (da Silva et al. 1994). As a result the wind curl has very low values, while alongshore winds have high values at the coast. The COADS-0.5° analysis shows quite similar overall magnitude for the wind stress but a different wind curl where coastal winds have lower values. There is much more difference among the analyses in the wind curl than in the wind stress. In particular, the alongshore, zero-wind-curl line in both COADS-1° and NCEP-1° lies around 300 km offshore, while the COADS-0.5° line lies closer

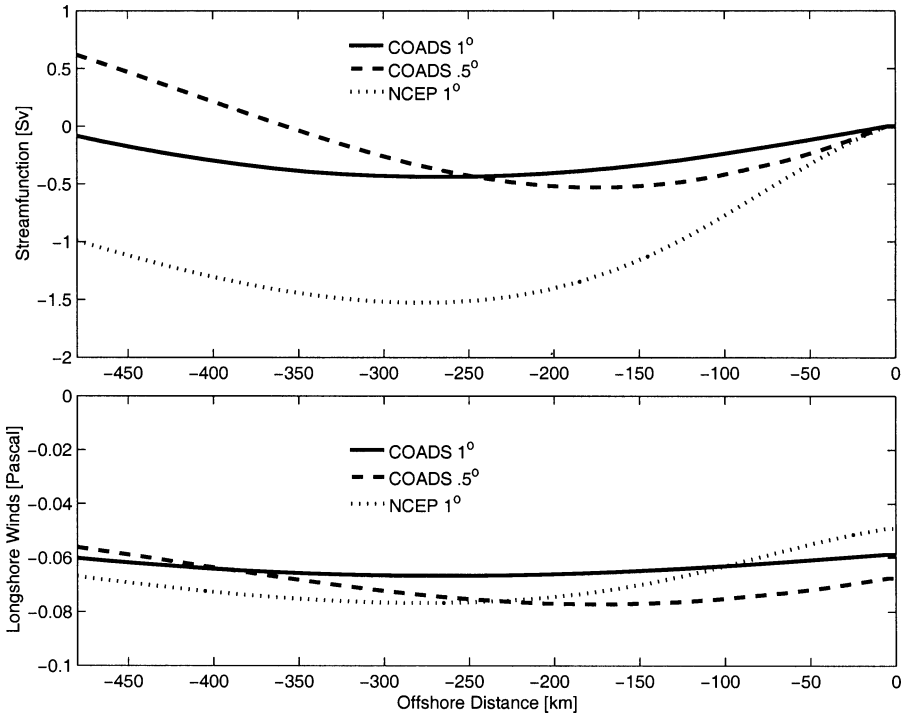

FIG. 18. Offshore profiles of annual-mean (top) Sverdrup streamlines and (bottom) alongshore wind stress for different wind forcings, averaged alongshore in the USWC upwelling region 34.5°–43°N.

to 150 km. The latter is more consistent with the estimates of Bakun and Nelson (1991) in this respect. [A recent wind study in the CCS region (J. Kindle 2001, personal communication) using the Coupled Ocean–Atmosphere Mesoscale Prediction System (COAMPS) indicates that the zero-wind-curl line may be even closer to the coast, with stronger associated wind curl and weaker alongshore winds in comparison with Bakun and Nelson (1991).]

Now we analyze the circulation and associated transport within 1000 m of the top surface.[2] In Fig. 19 (right panels) we see generally good agreement between the simulated upper ocean transport and Sverdrup transport for each of the three wind analyses. This clearly shows that, in spite of the nearby coastal boundary, the modeled mean offshore transport in the CCS is largely driven by Sverdrup dynamics [cf. section 4b(2)]. Among the different cross-shore profiles of alongshore currents (Fig. 19, left panels), we see differences associated with variations of the nearshore cyclonic wind curl in the width and transport of the subsurface poleward flow and its proximity to the surface. This reinforces the view (above) that both the strength of the DC and the possibility of it emerging at the surface during wind relaxation events are quite sensitive to the coastal wind curl. A similar relation exists between offshore equatorward currents and anticyclonic wind curl. The near-surface currents are only weakly sensitive to the wind curl itself, and they are more directly responsive to the coastal alongshore winds. Therefore, the wind curl alone has little effect on the seasonal variability of nearshore surface currents (Fig. 10), although the offshore surface flow does compare slightly better to the altimetric signal when forced with winds of higher resolution. In general, we conclude that the mean-seasonal currents in the CCS are sensitive to wind patterns that are still uncertainly estimated.

2) RESOLUTION EFFECTS

We use statistical results from three different simulations—at 5 km (fine), 10 km (medium), and 20 km (coarse)—to assess the effect of resolution on the CCS, as well as from the more briefly integrated solution with 3.5-km resolution. The effect on the mean alongshore currents and transports is shown in Fig. 20. There is an orderly change in the current structure from coarse to fine grids, with medium resolution giving intermediate results. The primary effect of a finer resolution is to intensify the coastal currents, though not to greatly change their spatial structure; for example, the CUC in the coarse grid model is only 3 cm s^{-1} compared with 5 cm s^{-1} in the fine-grid model. For the transports we see that the agreement with the cross-shore shape of the Sverdrup transport is closer at coarser resolution. The nonlinear processes, when better resolved, act to trap the CC shoreward while enhancing the offshore subsurface poleward flow. This is consistent with the results from heat and vorticity budgets. The heat budget reveals the role of eddy heat fluxes in trapping frontal formations and redistributing available potential energy [section 4d(3)]. The vorticity balance [section 4b(2)] shows that the alongshore transport is driven by both wind stress curl and transient and standing eddies. The eddy component is much weaker at lower resolution (not shown), leading to a simpler Sverdrup balance.

The resolution effect on mesoscale variability is presented in Fig. 21 and Table 1, which are time series and time-mean and mean-seasonal difference values for surface EKE averaged over the K98 domain; the latter are compared with the empirical estimates by Kelly et al. (1998). The equilibrium state is achieved at all resolutions but with very different EKE magnitudes. Even at the coarsest resolution there is evident interannual variability. Mean EKE almost doubles between coarse and medium resolutions, with a similar increase between medium and fine. The ratio of seasonal differences and annual mean for the coarse grid is 0.25, which increases significantly to 0.45 for the medium grid and 0.65 for the fine grid. The resolution sensitivity of the mean-seasonal circulation (not shown) is considerably smaller. Therefore, there is an increase with resolution not only of the mean EKE level but also the seasonally modulated, but nonseasonal (i.e., mesoscale), EKE variations. Since the eddy variability in these solutions occurs by instabilities of the coastal currents through shear and baroclinic instabilities, we conclude that the greater nearshore mean shears (Fig. 20) and the better resolution of the much larger shears near the instantaneous upwelling front and filaments (note that the baroclinic radius of deformation can become as small as 15 km in this region; Barth 1994) are important for simulating well the mesoscale fluctuations. In the coarse-grid simulation, frontal currents have maximum values of about 30 cm s^{-1} while they can reach about 1 m s^{-1} in the fine-grid simulation.

It is not evident from our solutions that a plateau has yet been reached for surface EKE when refining the resolution down to 5 km, although the model does produces a nearly realistic amount of EKE at this resolution [section 4d(1)]. We are currently analysing solutions from higher-resolution, equilibrium simulations (the 3.5-km simulation was not demonstrably run to its equilibrium) computed on a subdomain representing the central upwelling region nested in the larger USWC domain. Preliminary results support a leveling off of the EKE dependence on resolution below 5 km (Marchesiello et al. 2002). However, it is still unclear that the apparent convergence is due to a reduction of truncation errors. We have seen in section 4a that the 3.5-km sim-

[2] Below 1000 m, and particularly below 2000 m, there is a broad, weak (<0.5 cm s^{-1}), equatorward, abyssal circulation in our simulations. We choose to exclude the abyss from our analysis of the wind-driven circulation because of doubts about the adequacy of our vertical grid resolution and degree of temporal equilibration there.

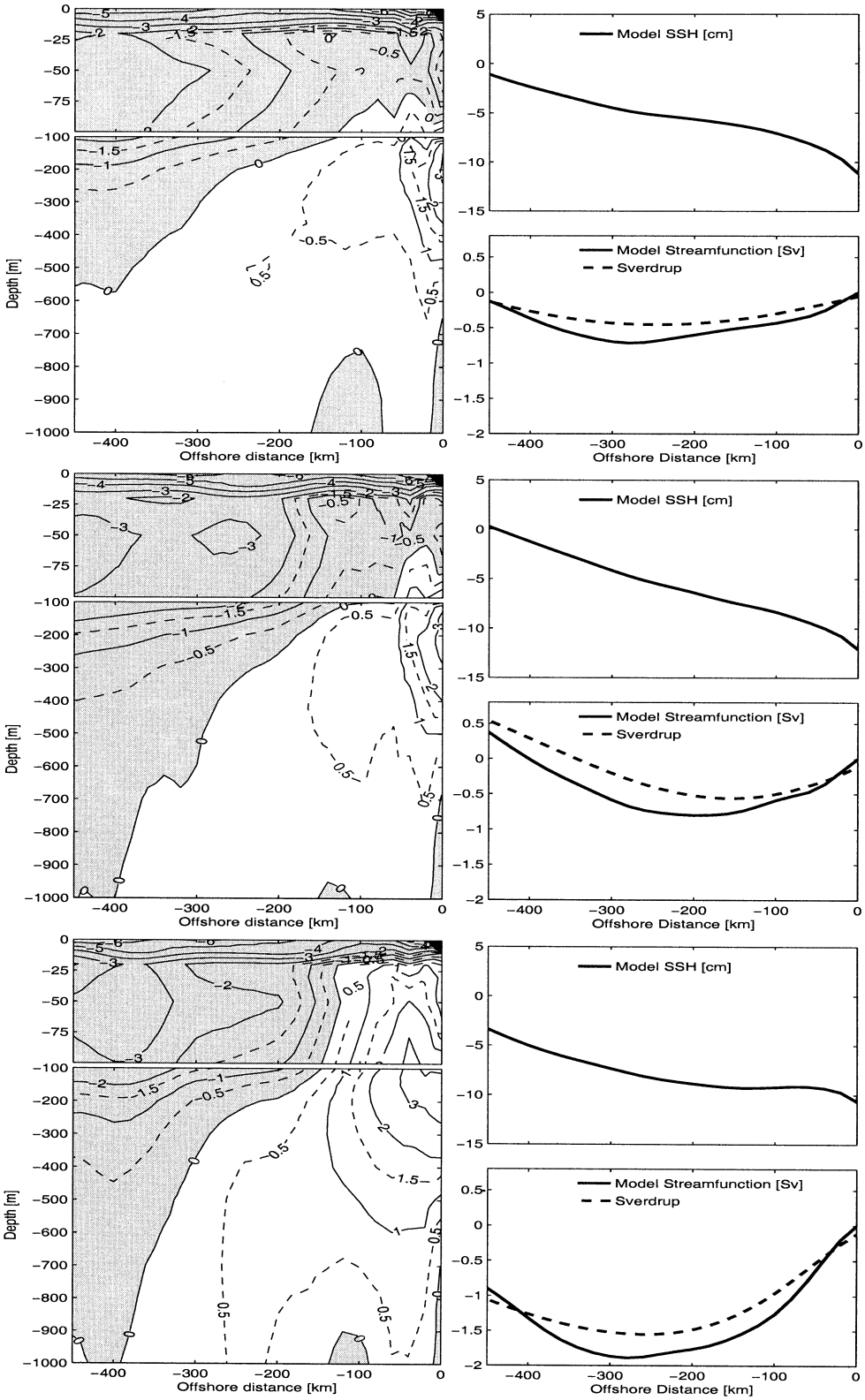

FIG. 19. Alongshore currents, SSH, and transports in the USWC upwelling region 34.5°–43°N for different winds from the model with 20-km resolution: COADS-1° resolution, COADS-0.5°, and NCEP-1°. (left) Alongshore currents [CI = 1 cm s^{-1}; dashed lines are (−1.5, −0.5, 0.5, 1.5) contour values, and regions of negative flow are shaded]. (right) SSH (cm) and streamfunction (Sv). The figure compares solutions from the model with the Sverdrup transport.

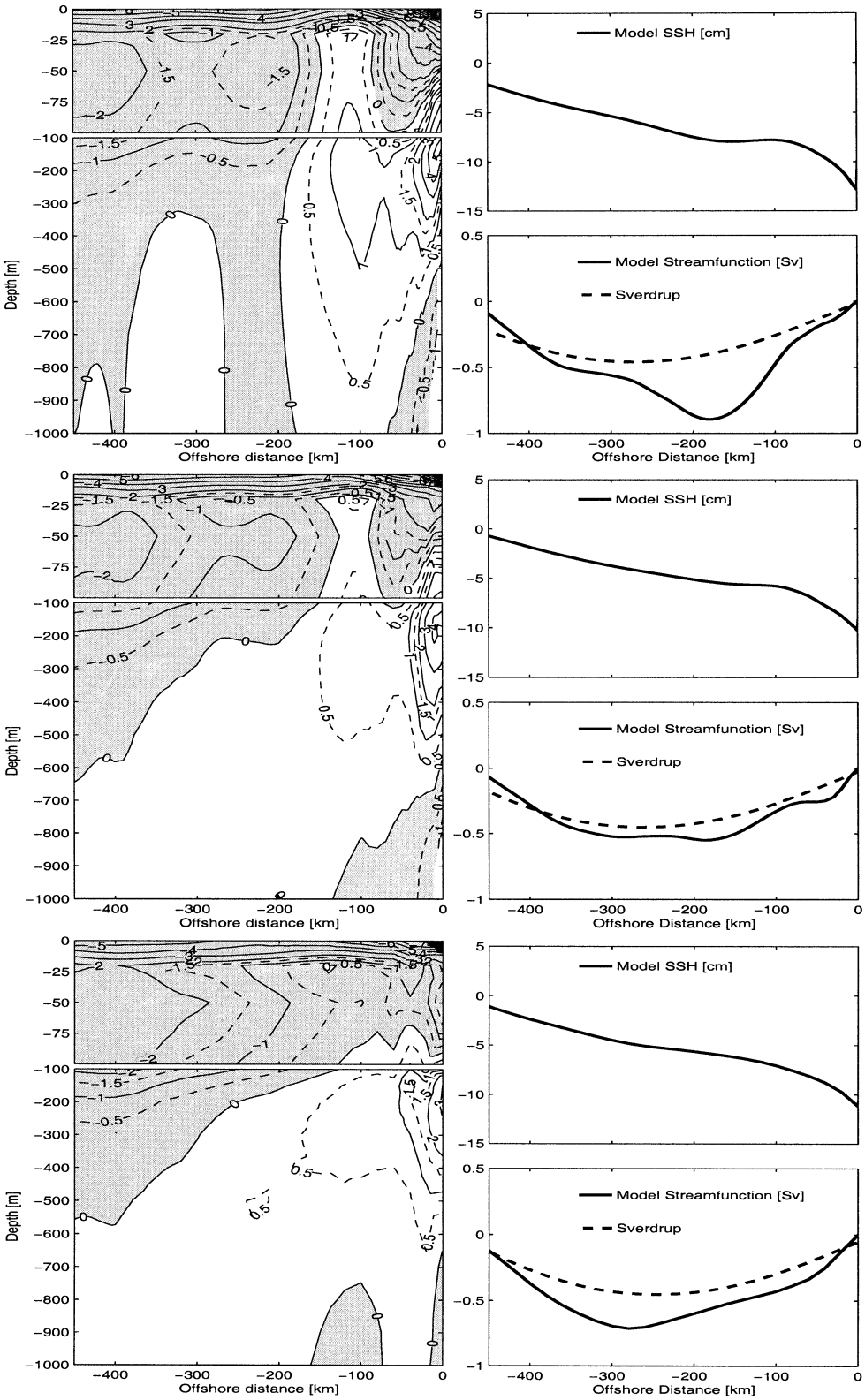

FIG. 20. Alongshore currents, SSH, and transports in the USWC upwelling region (34.5°–43°N) at different horizontal resolutions [(top) 5 km (middle) 10 km, (bottom) 20 km] for COADS-1° wind forcing. (left) Alongshore currents [CI = 1 cm s^{-1}; dashed lines are (−1.5, −0.5, 0.5, 1.5) contour values, and regions of negative flow are shaded]. (right) SSH (cm) and streamfunction (Sv). The figure compares solutions from the model with the Sverdrup transport.

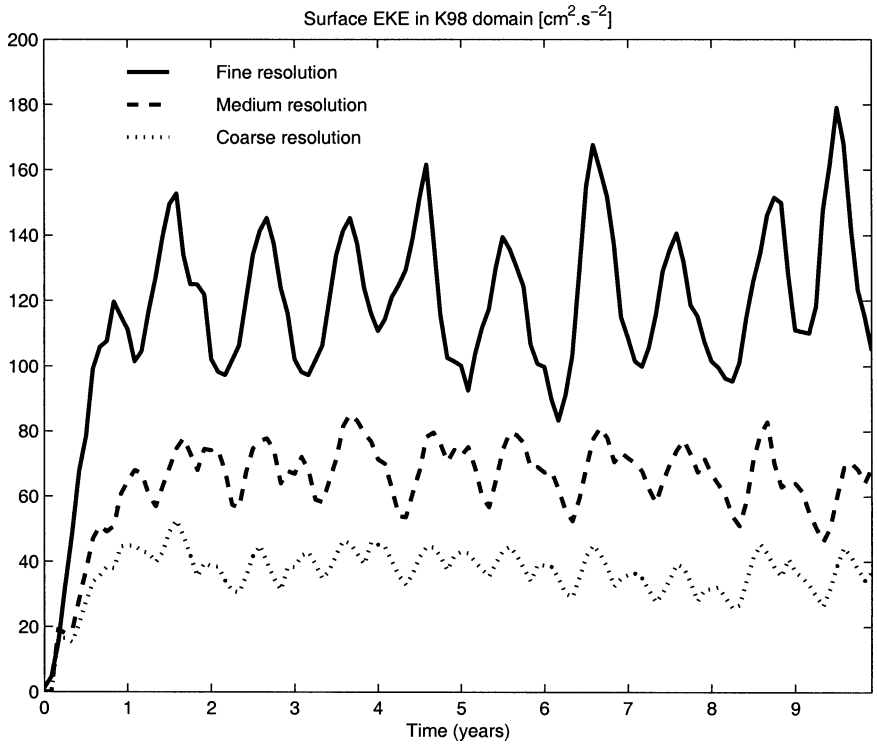

FIG. 21. Time evolution of the surface KE in the domain (33°–40.5°N, 124°–132°W) at three different resolutions: 5, 10, and 20 km.

ulation appears to show an unstable mode pattern not present in the coarser simulations. It appears as a rapidly growing, surface-trapped, short-wavelength frontal mode, similar to the ageostrophic, unstable modes described by McCreary et al. (1991), Barth (1994), and Fukamachi et al. (1995), associated by them with small-scale patterns commonly observed from satellite on upwelling fronts and jets in different coastal regions. These modes require strong anticyclonic shears, comparable to f. This condition occurs in the 3.5-km solution on the upwelling fronts and filaments. Thus, our present results also suggest the possibility of a transition regime as the grid resolution is enhanced where such frontal instabilities start to impact on coastal currents and offshore mesoscale eddies. But for now we can merely advance this as a conjecture, pending higher-resolution, equilibrium simulations to check its validity.

3) CAPES AND RIDGES

The simulations show standing eddies and EKE extrema around capes and ridges. To assess the influence of these topographic features, we present several solutions at coarse resolution (20 km) to compare the standard case with two flat-bottom cases, one with the standard coastline and the other with a nearly straight coastline (Fig. 22). The mean SSH in the flat-bottom case does not show the large-scale standing eddies observed in the standard case; instead, only smaller-scale meanders are trapped by the different capes. Its EKE also has enhanced values at capes, especially near Cape Mendocino with an offshore maximum twice as large as in the standard case. In the flat-bottom/straight-coast case, the meandering almost completely disappears (what remains is likely sampling error due to the finite averaging time). The EKE retains its large amplitude near the coast, but it is now smoothly spread over the entire upwelling region with limited offshore extension. In this case, filaments and eddies are still formed but not anchored to particular locations.

These experiments demonstrate two different influences of topography on the eddy flow. First, the enhanced EKE produced by capes in the absence of topography confirm the results of Batteen (1997), who compares solutions analogous to the flat-bottom and flat-bottom/straight-coast cases here. However, in our standard case with irregular coastline and topography, lower values of eddy energy occur compared to the flat-bottom case. The continental slope appears to stabilize coastal upwelling currents and limit the effect of alongshore variations in topography and coastline configuration. In quasigeostrophic models, sloping bottom topography does stabilize the upwelling fronts in the sense that the growth rates are smaller (Barth 1989). Secondly, ridges and capes cause the generation of large-scale standing meanders in the CCS, as also found in laboratory experiments (Narimousa and Maxworthy 1989). In Fig. 22, we see that the location of Cape Mendocino, with

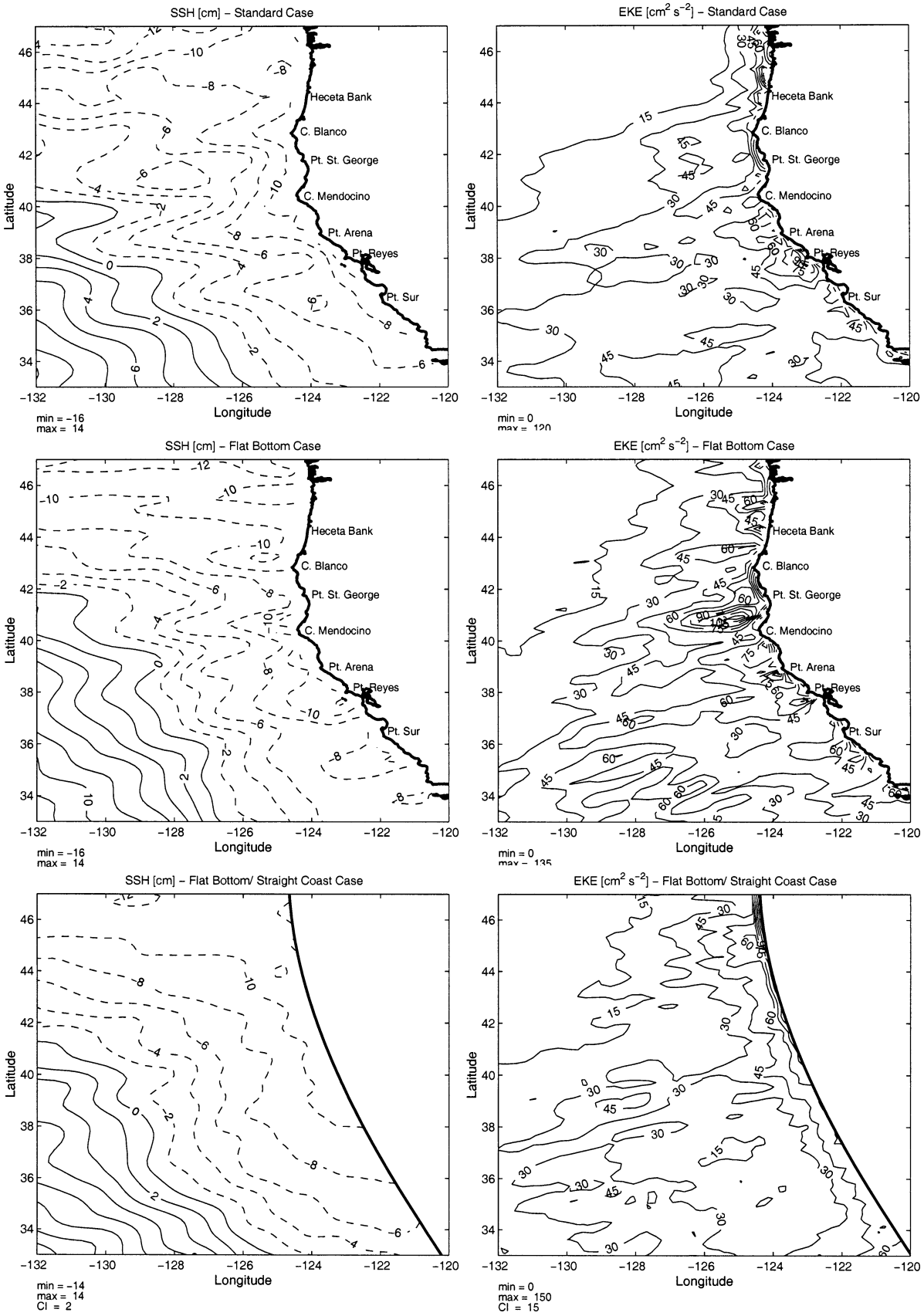
SSH [cm] – Standard Case
EKE [cm^2 s^{-2}] – Standard Case
SSH [cm] – Flat Bottom Case
EKE [cm^2 s^{-2}] – Flat Bottom Case
SSH [cm] – Flat Bottom/ Straight Coast Case
EKE [cm^2 s^{-2}] – Flat Bottom/ Straight Coast Case
Heceta Bank
C. Blanco
Pt. St. George
C. Mendocino
Pt. Arena
Pt. Reyes
Pt. Sur
Latitude
Longitude
min = −16
max = 14
min = 0
min = −14
max = 14
CI = 2
max = 150
CI = 15

its sharp escarpment, is favorable to the generation of the largest such standing waves, and it seems likely that downstream instabilities may thereby be altered (e.g., at Point Arena). According to Narimousa and Maxworthy, the variability at Point Arena is associated with instabilities of standing waves generated at Cape Mendocino rather than instabilities of local upwelling jets. This interpretation is consistent with our results and implies that a local model of the Point Arena region might not be suitable for producing realistic eddy flows.

4) Coriolis gradient

It is still common practice to study coastal jets neglecting β, the meridional gradient of the Coriolis frequency (Oke et al. 2002; Barth 1994; Haidvogel et al. 1991). Batteen (1997) and McCreary and Kundu (1985) show that the formation of meanders, eddies, and filaments in eastern-boundary current systems is conditioned by the horizontal and vertical structure of coastal currents, and an important effect of β is to produce alongshore pressure gradients that aid the generation of realistic shears. In the $\beta = 0$ solution of Batteen (1997), the surface equatorward coastal current is too strong and deep (i.e., with a strong equatorward barotropic component), and the undercurrent is too weak and deep (extending over $\sim$1000 m instead of $\sim$300 m); this structure is not favorable for instability, especially when the model is forced with steady winds (temporal variability in wind forcing can also enhance vertical and horizontal shears). However, these conclusions were made with a flat-bottom model, and role of the topography in generating alongshore pressure gradients was not investigated. We have also made a $\beta = 0$ experiment with the USWC configuration at coarse resolution (20 km). In this case (not shown), the upwelling front and associated coastal jet meander with only limited cross-shore extension while not creating the cutoff eddies, squirts, and cold filaments present in the standard solutions nor exhibiting the pervasive westward propagation in the seasonal cycle. The coastal jet with $\beta = 0$ is strong and deep with a strong barotropic component (equatorward), and the undercurrent is deep and weak compared to the standard case. These results are similar to Batteen's except for the small meandering around capes and ridges. We conclude that the common use of a periodic meridional channel, where $\beta = 0$ is a necessary choice, is inappropriate for modeling the intrinsic mesoscale variability across the continental slope because it does not produce realistic coastal currents. [Haidvogel et al. (1991) partly overcome this problem by imposing the horizontal and vertical shears in the coastal currents at the northern and southern boundaries so that the instability leads to more realistic turbulent behavior, but this boundary condition is not appropriate for a simulation of the CCS as whole.]

Alongshore pressure gradients also have a great influence on the vertical upwelling cell. They support onshore return currents within the interior of the water column, rather than only within the bottom boundary layer (Marchesiello et al. 2000). Interior onshore flows have been observed and associated with alongshore pressure gradients in the CCS (Federiuk and Allen 1995), and our simulations also show this structure (Fig. 7). In contrast, in western-boundary current systems, the β effect may counteract the formation of alongshore pressure gradients, undercurrents, and interior onshore flows (McCreary and Kundu 1985; Marchesiello and Middleton 2000).

5. Conclusions

We present simulations of the regional California Current System off the U.S. West Coast using ROMS. Under the influences of mean-seasonal atmospheric forcing and subtropical-gyre open boundary conditions, a robust equilibrium state is established on a time scale of a few years. It has mean alongshore and cross-shore currents similar to those estimated from hydrographic climatologies, and it also has vigorous, deep, standing-eddy patterns associated with capes and subsurface ridges along the coast. Its large-scale and mean-seasonal circulation and sea level structure are relatively insensitive to resolution refinements below a horizontal grid scale of 20 km (coarser grids were not examined). However, the more sensitive standing eddies and transient eddies do modulate the classical Sverdrup balance within the coastal transition zone. The CCS has large seasonal anomalies (also as observed), driven by seasonal wind variations and propagating offshore at a Rossby wave speed accompanied by seasonal anomalies in eddy kinetic energy whose vertical extent also deepens moving offshore. The annual- and seasonal-mean circulations exhibit strong intrinsic variability, generated mainly by baroclinic instability of the persistent currents except very near the coastline where lateral shear instability is also important. The variability is primarily mesoscale, geostrophic currents, although there is a nonnegligible ageostrophic component in the surface boundary layer and near the coast. The geographical distribution of this mesoscale variability is similar to those observed in sea level and surface currents, and at the finer model resolutions the variance magnitudes are nearly as large as observed. The mesoscale synoptic structure is a combination of upwelling fronts, offshore squirts and filaments, and eddies, many of which occur as dipoles. The

←

Fig. 22. Time-mean SSH and surface EKE from the model with 20-km resolution: (top) standard configuration; (middle) flat-bottom, standard coastline; and (bottom) flat-bottom, smooth coastline.

eddies provide an important dissipation mechanism for the mean circulation through instabilities (although not as important as radiation into the subtropical gyre interior) and the prevalent, alongshore, coastal T and S gradient is maintained by eddy heat fluxes limiting the mean, wind-driven, upwelling advection. Last, by performing alternative simulations selectively subtracting various model elements, we have demonstrated the significant influences of coastline shape, topographic variations in the nearshore region, and the gradient of the Coriolis frequency through its effects on the alongshore pressure gradient, mean current shears, and the general westward progression in the CCS.

The least satisfactory aspect of these simulations is the sensitivity of even the large-scale circulation (especially the Davidson Current) to uncertainties in the large-scale, low-frequency wind analyses used to force the model. The biggest qualitative discrepancy between these simulations and observations occurs for the seasonal and mesoscale SSH variability and EKE (and also SST variance, not presented here) very near the coast and especially near capes. Wind errors are likely to be a significant cause of this model bias, because the large-scale analyses lack known small-scale orographic features. In addition, this is a shelf and slopewave regime where transient wind forcing (missing here) is effective in exciting local response (Allen 1980; Brink 1991). Last, we have seen that our simulations may be near a resolution threshold with respect to nearshore, small-scale, ageostrophic instabilities, whose role has yet to be determined. Thus, important directions for further research are toward more accurate, finer-scale wind forcing and better spatial resolution in the nearshore region.

We intentionally posed our calculations here without synoptic and interannual forcing, in order to expose the central role of intrinsic variability in the CCS. The successes of the simulations, in approximately matching much of the available observations, suggest that the large-scale structure of the CCS is substantially a deterministic response to the low-frequency, large-scale atmospheric forcing—whether local or remote and transmitted through the regional boundaries—while the mesoscale variability is intrinsic, hence chaotic with limited predictability. Yet this variability is an essential ingredient in establishing the structure and conducting the dynamics of the CCS.

Acknowledgments. We appreciate financial support from ONR (N00014-00-1-0249), NASA (NAG5-9860), EPA (R825381), and California Sea Grant (R/CZ-171). Computations were made at NCSA, which is sponsored by NSF. We also thank Ted Strub and Dylan Righi who provided the satellite altimeter analysis, and Peter Niiler who provided the drifters analysis.

REFERENCES

Allen, J. S., 1980: Models of wind-driven currents on the Continental Shelf. *Ann. Rev. Fluid Mech.,* **12,** 389–433.

Auad, G., A. Pares-Sierra, and G. K. Vallis, 1991: Circulation and energetics of a model of the California Current system. *J. Phys. Oceanogr.,* **21,** 1534–1552.

Bakun, A., and C. S. Nelson, 1991: The seasonal cycle of wind-stress curl in subtropical eastern boundary current regions. *J. Phys. Oceanogr.,* **21,** 1815–1834.

Barnier, B., L. Siefried, and P. Marchesiello, 1995: Thermal forcing for a global ocean circulation model using a three-year climatology of ECMWF analyses. *J. Mar. Syst.,* **6,** 363–380.

——, P. Marchesiello, A. Pimenta de Miranda, M. Coulibaly, and J. M. Molines, 1998: A sigma-coordinate primitive equation model for studying the circulation in the South Atlantic. Part I: Model configuration with error estimates. *Deep-Sea Res.,* **45A,** 543–572.

Barth, J. A., 1989: Stability of a coastal upwelling front. 1. Model development and a stability theorem. *J. Geophys. Res.,* **94,** 10 844–10 856.

——, 1994: Short-wavelength instabilities on coastal jest and fronts. *J. Geophys. Res.,* **99,** 16 095–16 115.

——, S. D. Pierce, and R. L. Smith, 2000: A separating coastal upwelling jet at Cape Blanco, Oregon and its connection to the California Current System. *Deep-Sea Res.,* **47B,** 783–810.

Batteen, M. L., 1997: Wind-forced modeling studies of currents, meanders, and eddies in the California Current system. *J. Geophys. Res.,* **102,** 985–1010.

Beckmann, A., and D. B. Haidvogel, 1993: Numerical simulation of flow around isolated seamount. Part I: Problem formulation and model accuracy. *J. Phys. Oceanogr.,* **23,** 1736–1753.

Blumberg, A. F., and G. L. Mellor, 1987: A description of a three-dimensional coastal ocean circulation model. *Three Dimensional Ocean Models,* N. Heaps, Ed., Amer. Geophys. Union, 208 pp.

Brink, K. H., 1991: Coastal-trapped waves and wind-driven currents over the continental shelf. *Ann. Rev. Fluid Mech.,* **23,** 389–412.

——, 1998: The global coastal ocean: Processes and methods. *The Sea,* K. H. Brink and A. R. Robinson, Eds., Vol. 10, Chap. 6, John Wiley and Sons, 604 pp.

Charney, J. G., 1971: Geostrophic turbulence. *J. Atmos. Sci.,* **28,** 1087–1095.

Chelton, D. B., 1984: Seasonal variability of alongshore geostrophic velocity off central California. *J. Geophys. Res.,* **89,** 3473–3486.

——, and M. G. Schlax, 1996: Global observations of oceanic Rossby waves. *Science,* **272,** 234–238.

Chereskin, T. K., M. Y. Morris, P. P. Niiler, P. M. Kosro, R. L. Smith, S. R. Ramp, C. A. Collins, and D. L. Musgrave, 2000: Spatial and temporal characteristics of the mesoscale circulation of the California Current from eddy-resolving moored and shipboard measurements. *J. Geophys. Res.,* **105,** 1245–1269.

Cornuelle, B., T. K. Chereskin, P. P. Niiler, and M. Y. Morris, 2000: Observations and modeling of a California undercurrent eddy. *J. Geophys. Res.,* **105,** 1227–1243.

da Silva, A., C. Young, and S. Levitus, 1994: *Atlas of Surface Marine Data 1994.* Vols. 1–5. NOAA Atlas NESDIS 6-10, U.S. Government Printing Office.

Enriquez, A. G., and C. A. Friehe, 1995: Effects of wind stress and wind stress curl variability on coastal upwelling. *J. Phys. Oceanogr.,* **25,** 1651–1671.

Federiuk, J., and J. S. Allen, 1995: Upwelling circulation on the Oregon continental shelf. Part II: Simulations and comparisons with observations. *J. Phys. Oceanogr.,* **25,** 1867–1889.

Fukamachi, Y., J. P. McCreary, and J. A. Proehl, 1995: Instability of density fronts in layered and continuously stratified models. *J. Geophys. Res.,* **100,** 2559–2577.

Haidvogel, D. B., A. Beckmann, and K. S. Hedstrom, 1991: Dynamical simulations of filament formation and evolution in the coastal transition zone. *J. Geophys. Res.,* **96,** 15 017–15 040.

Haney, R. L., R. A. Hale, and D. E. Dietrich, 2001: Offshore propagation of eddy kinetic energy in the California Current. *J. Geophys. Res.,* **106,** 11 709–11 718.

Harrison, D. E., and A. R. Robinson, 1978: Energy analysis of open

regions of turbulent flows: mean eddy energetics of a numerical ocean circulation experiment. *Dyn. Atmos. Oceans,* **2,** 185–211.
Hickey, B. M., 1979: The California Current System—Hypothesis and facts. *Progress in Oceanography,* Vol. 8, Pergamon, 191–279.
——, 1992: Circulation over the Santa Monica–San Pedro basin and shelf. *Progress in Oceanography,* Vol. 30, Pergamon, 37–115.
——, 1998: Coastal oceanography of western North America from the tip of Baja California to Vancouver Island: Coastal segment. *The Sea,* A. R. Robinson and K. H. Brink, Eds., Vol. 11, John Wiley and Sons, 345–391.
Ikeda, M., L. A. Mysak, and W. J. Emery, 1984: Observation and modeling of satellite-sensed meanders and eddies of Vancouver Island. *J. Phys. Oceanogr.,* **14,** 3–21.
Kelly, K. A., R. C. Beardsley, R. Limeburner, K. H. Brink, J. D. Paduan, and T. K. Chereskin, 1998: Variability of the near-surface eddy kinetic energy in the California Current based on altimetric, drifter, and moored current data. *J. Geophys. Res.,* **103,** 13 067–13 083.
Lagerloef, G. S., 1992: The Point Arena eddy: A recurring summer anticyclone in the California Current. *J. Geophys. Res.,* **97,** 12 557–12 568.
Large, W. G., and P. R. Gent, 1999: Validation of vertical mixing in an equatorial ocean model using large eddy simulations and observations. *J. Phys. Oceanogr.,* **29,** 449–464.
——, J. C. McWilliams, and S. C. Doney, 1994: Oceanic vertical mixing: A review and a model with a nonlocal boundary layer parameterization. *Rev. Geophys.,* **32,** 363–403.
Levitus, S., and T. P. Boyer, 1994: *Temperature.* Vol. 4, *World Ocean Atlas 1994,* NOAA Atlas NESDIS 4, 117 pp.
——, R. Burgett, and T. P. Boyer, 1994: *Salinity.* Vol. 3, *World Ocean Atlas 1994,* NOAA Atlas NESDIS 3, 99 pp.
Li, X., Y. Chao, J. C. McWilliams, and L.-L. Fu, 2001: A comparison of two vertical mixing schemes in a Pacific Ocean General Circulation Model. *J. Climate,* **14,** 1377–1398.
Lott, F., G. Madec, and J. Verron, 1990: Topographic experiments in an ocean general circulation model. *Ocean Modelling,* **88.**
Lynn, R., and J. J. Simpson, 1987: The California Current system: The seasonal variability of its physical characteristics. *J. Geophys. Res.,* **92,** 12 947–12 966.
Marchesiello, P., and J. H. Middleton, 2000: Modeling the East Australian Current in the Western Tasman Sea. *J. Phys. Oceanogr.,* **30,** 2956–2971.
——, B. Barnier, and A. Pimenta de Miranda, 1998: A sigma-coordinate primitive-equation model for studying the circulation in the South Atlantic. Part II: Meridional transports and seasonal variability. *Deep-Sea Res.,* **45A,** 573–608.
——, M. T. Gibbs, and J. Middleton, 2000: Simulations of coastal upwelling on the Sydney continental shelf. *Mar. Freshwater Res.,* **51,** 577–588.
——, J. C. McWilliams, and A. Shchepetkin, 2001: Open boundary conditions for long-term integration of regional oceanic models. *Ocean Modell.,* **3,** 1–20.
——, ——, K. Stolzenbach, and N. Gruber, 2002: Equilibrium physical and ecosystem dynamics of the California Current System. *Investigationes Marinas, Proc. of the El Niño Symp. and Workshop,* Viña del Mar, Chile, Catholic University of Valparaiso, 96–98.
McCreary, J. P., and P. K. Kundu, 1985: Western boundary circulation driven by an alongshore wind: With application to the Somali Current system. *J. Mar. Res.,* **43,** 493–516.
——, ——, and S.-Y. Chao, 1987: On the dynamics of the California Current system. *J. Mar. Res.,* **45,** 1–32.
——, Y. Fukamachi, and P. K. Kundu, 1991: A numerical investigation of jets and eddies near an eastern ocean boundary. *J. Geophys. Res.,* **96,** 2515–2534.
McWilliams, J. C., J. B. Weiss, and I. Yavneh, 1994: Anisotropy and coherent structures in planetary turbulence. *Science,* **264,** 410–413.
Mied, R. P., J. C. McWilliams, and G. J. Lindemann, 1991: The generation and evolution of mushroomlike vortices. *J. Phys. Oceanogr.,* **21,** 489–510.
Munk, W. H., 1950: On the wind driven ocean circulation. *J. Meteor.,* **7,** 79–93.
Narimousa, S., and T. Maxworthy, 1989: Application of a laboratory model to the interpretation of satellite and field observations of coastal upwelling. *Dyn. Atmos. Ocean.,* **13,** 1–46.
NGDC, 1988: *Data Announcement 88-MG-02: Digital Relief of the Surface of the Earth.* NOAA, National Geophysics Data Center, CD-ROM.
Oke, P. R., J. S. Allen, R. N. Miller, G. D. Egbert, and P. M. Kosro, 2002: Assimilation of surface velocity data into a primitive equation coastal ocean model. *J. Geophys. Res.,* **107,** 3122, doi: 10.1029/2000JC000511.
Pares-Sierra, A., W. B. White, and C.-K. Tai, 1993: Wind-driven coastal generation of annual mesoscale eddy activity in the California Current system: A numerical model. *J. Phys. Oceanogr.,* **23,** 1110–1121.
Parrish, D. F., and J. C. Derber, 1992: The National Meteorological Center's spectral statistical interpolation analysis system. *Mon. Wea. Rev.,* **120,** 1747–1763.
Paulson, C. A., and J. J. Simpson, 1977: Irradiance measurements in the upper ocean. *J. Phys. Oceanogr.,* **7,** 952–956.
Pierce, S. D., R. L. Smith, P. M. Kosro, J. A. Barth, and C. D. Wilson, 2000: Continuity of the poleward undercurrent along the eastern boundary of the mid-latitude North Pacific. *Deep-Sea Res.,* **47B,** 811–829.
Rhines, P. B., 1979: Geostrophic turbulence. *Ann. Rev. Fluid Mech.,* **11,** 401–411.
Sanderson, B. G., 1998: Order and resolution for computational ocean dynamics. *J. Phys. Oceanogr.,* **28,** 1271–1286.
Shchepetkin, A., and J. C. McWilliams, 1998: Quasi-monotone advection schemes based on explicit locally adaptive dissipation. *Mon. Wea. Rev.,* **126,** 1541–1580.
——, and ——, 2003: A method for computing horizontal pressure-gradient force in an oceanic model with a non-aligned vertical coordinate. *J. Geophys. Res.,* in press.
Simpson, J. J., and R. J. Lynn, 1990: A mesoscale eddy dipole in the offshore California Current. *J. Geophys. Res.,* **95,** 13 009–13 022.
Song, Y. T., 1998: A general pressure gradient formulation for ocean models. Part I: Scheme design and diagnostic analysis. *Mon. Wea. Rev.,* **126,** 3213–3230.
——, and D. B. Haidvogel, 1994: A semi-implicit ocean circulation model using a generalized topography following coordinate system. *J. Comput. Phys.,* **115,** 228–248.
Strub, P. T., and C. James, 2000: Altimeter derived variability of surface velocities in the California Current System: 2. Seasonal circulation and eddy statistics. *Deep-Sea Res. II,* **47B,** 831–870.
——, P. M. Kosro, and A. Huyer, 1991: The nature of the cold filaments in the California Current System. *J. Geophys. Res.,* **96,** 14 743–14 768.
Sverdrup, H. U., 1947: Wind-driven currents in a baroclinic ocean; with application to the equatorial currents of the eastern Pacific. *Proc. Natl. Acad. Sci.,* **33,** 318–326.
Swenson, M. S., and P. P. Niiler, 1996: Statistical analysis of the surface circulation of the California Current. *J. Geophys. Res.,* **101,** 22 631–22 645.
Taylor, P. K., Ed., 2000: Intercomparison and validation of ocean–atmosphere energy flux fields. Joint WCRP/SCOR Working Group on Air–Sea Fluxes, Southampton Oceanography Centre, 306 pp.
Thompson, R. E., and J. E. Papadakis, 1987: Upwelling filaments and motion of satellite-tracked drifter along the west coast of North America. *J. Geophys. Res.,* **92,** 6445–6461.
Wyllie, J. G., 1966: Geostrophic flow of the California Current at the surface and at 200 m. *CalCOFI Atlas,* Scripps Institution of Oceanography, 48 pp. and 288 charts.